






## RESEARCH ARTICLE

10.1029/2023JD039708

## Air-Sea Heat Fluxes Associated With Convective Cold Pools

Samantha M. Wills<sup>1,2</sup> , Meghan F. Cronin<sup>2</sup> , and Dongxiao Zhang<sup>1,2</sup> 

<sup>1</sup>Cooperative Institute for Climate, Ocean, and Ecosystem Studies, University of Washington, Seattle, WA, USA, <sup>2</sup>Pacific Marine Environmental Laboratory, NOAA, Seattle, WA, USA

### Key Points:

- High-resolution uncrewed surface vehicles measurements provide new insight on sub-grid/sub-footprint variability associated with convective cold pools
- Convective cold pool fronts modulate latent heat fluxes primarily through mechanical forcing by the anomalous wind field
- Convective cold pool fronts modulate sensible heat fluxes primarily through thermodynamic forcing by the anomalous temperature gradient

### Supporting Information:

Supporting Information may be found in the online version of this article.

### Correspondence to:

S. M. Wills,  
[smwills@uw.edu](mailto:smwills@uw.edu)

### Citation:

Wills, S. M., Cronin, M. F., & Zhang, D. (2023). Air-sea heat fluxes associated with convective cold pools. *Journal of Geophysical Research: Atmospheres*, 128, e2023JD039708. <https://doi.org/10.1029/2023JD039708>

Received 26 JUL 2023  
Accepted 5 OCT 2023

**Abstract** High-resolution air-sea observations collected by a suite of remotely-piloted uncrewed surface vehicles (USV) provide new insight on surface latent and sensible heat fluxes associated with convective cold pools over the eastern Pacific Intertropical Convergence Zone (ITCZ). Convective cold pools are linked to isolated, heavily precipitating cells over the ocean that yield downdrafts of evaporatively-cooled air that spreads out horizontally in all directions and are characterized by strong air temperature gradients and horizontal wind speeds. Cold pool frontal signatures are identified based on air temperature depression criteria of  $-1.5^{\circ}\text{C}$  in 10 min or less, resulting in a total of 276 events observed within the eastern Pacific ITCZ across 590 total seadays of data from 10 drones over the course of 3 years. Composite analysis reveals enhanced latent and sensible heat fluxes from the ocean to the atmosphere immediately following the frontal passage, and a decomposition of the bulk flux formulas indicates that variations in latent heat flux are largely influenced by the anomalous wind field (i.e., the cold pool gust front) acting on the mean background air-sea moisture gradient, while variations in sensible heat flux are largely influenced by the mean background wind acting on the anomalous air-sea temperature gradient (i.e., the cold pool temperature front). High-frequency variations in wind speed and velocity are further explored in the context of “gustiness” and averaging intervals used in bulk flux algorithms. A case study is also presented for a convective cold pool event captured by a traveling mesoscale network, or mesonet, of USVs.

**Plain Language Summary** New 1-min measurements of oceanic and atmospheric variables collected by automated observing platforms, Sairdrone uncrewed surface vehicles, are used to explore convective cold pools over the stormy region of the northern hemisphere eastern tropical Pacific ocean. Convective cold pools are domes of cold air near the surface that form underneath intensely raining thunderstorms. The cold pool boundary (or front) separates the cold, dry air within the dome from the warm, moist air of the surrounding environment, and thus qualifying events are identified based on temperature drops of  $-1.5^{\circ}\text{C}$  in 10 min or less in the 1-min saildrone data. Results based on 276 cold pool events observed between 10 drones over 3 years reveal that increasing wind speed and decreasing air temperature associated with the cold pool front largely contribute to enhanced air-sea heat fluxes (i.e., exchanges of energy) from the ocean to the atmosphere, highlighting the importance of high-resolution (i.e., 1-min) observations to capture variations on small time and space scales. A cold pool event observed by multiple saildrones is also explored, and wind measurements from a single saildrone are further investigated in the context of a “gustiness” parameter used in the bulk flux equations.

## 1. Introduction

The near-surface wind, temperature, and humidity fields over the tropical ocean exhibit large variability on sub-grid scales not currently resolved within most global climate model (GCM) and satellite footprints. Sub-grid scale variability refers to spatial and temporal distributions of local, small-scale processes within a grid box that are often represented through parameterizations rather than physical quantities. High-frequency (i.e., minutes to hours) variations in wind, temperature, and humidity over the tropical ocean are often associated with convective activity that occurs on meso-gamma ( $\sim 10$  km) and meso-beta ( $\sim 100$  km) scales, such as atmospheric cold pools that form under precipitating clouds (Benjamin, 1968; Byers & Braham, 1949; Houze, 1977; Williams, 2001; Zipser, 1969). Cold pools occur when evaporatively-cooled air sinks to the surface and expands horizontally in all directions, resulting in local air temperature and moisture fronts that alter the surrounding environment (Betts & Silva Dias, 1979; Fournier & Haerter, 2019; Glickman & Zenk, 2000; Haerter & Schlemmer, 2018; Lafore & Moncrieff, 1989; Rochetin et al., 2021; Tompkins, 2001). These frontal regions are also accompanied by large variations in wind speed (i.e., the “gust” front) that drive air-sea fluxes, or surface exchanges of energy between

© 2023 The Authors. This article has been contributed to by U.S. Government employees and their work is in the public domain in the USA.

This is an open access article under the terms of the [Creative Commons Attribution License](https://creativecommons.org/licenses/by/4.0/), which permits use, distribution and reproduction in any medium, provided the original work is properly cited.

the ocean and the atmosphere (Garg et al., 2020, 2021; Grant & van den Heever, 2016; Gentine et al., 2016; Langhans & Romps, 2015; Ross et al., 2004; Saxen & Rutledge, 1998; Skyllingstad & de Szoeke, 2015; Young et al., 1995).

Gust fronts associated with atmospheric cold pools are characterized as periods of enhanced winds that can either immediately precede or follow behind the leading edge of the temperature front. While a wind gust is defined by the World Meteorological Organization as the “maximum value, over the observing cycle, of the 3-s running average wind speed,” the term *gust* is relative and can be applied over other finite time intervals. Here, we refer to the gust front as the initial period of increased wind speeds relative to pre-frontal conditions, which has been found to lead the temperature front in some cases (Byers & Braham, 1949; Drager & van den Heever, 2017; van den Heever et al., 2021). Importantly, a period of peak wind speed anomalies trails behind the leading edge of the gust front boundary, typically occurring 5–10 min after the beginning of the temperature front (Chandra et al., 2018; de Szoeke et al., 2017; Wills et al., 2021; Zuidema et al., 2017). This feature arises due to the radial expansion of relatively high-pressure air within the cold, dry air dome, propagating outward like a density current with phase speeds that sometimes better match those of higher-order gravity waves (Benjamin, 1968; Charba, 1974; Goff, 1976; Grant et al., 2018; Moncrieff & Liu, 1999; Wakimoto, 1982). An early study by Simpson (1969) found that the propagation speed of a sea-breeze or haboob is a function of the temperature perturbation, and recent studies suggest a positive relationship between horizontal wind speeds and strong air temperature gradients associated with convective cold pools, or cold pools linked to isolated, heavily precipitating convective cells (Feng et al., 2015; Garg et al., 2020; Kilpatrick & Xie, 2015; Schiro & Neelin, 2018). These convective cold pools and their gust fronts influence the near-surface boundary layer through a competition of mechanical and thermodynamic forcings and have important implications for modulating local air-sea fluxes of heat and momentum (Chuda et al., 2008; Li et al., 2014; Tompkins, 2001; Torri et al., 2015).

Air-sea heat fluxes are often calculated using bulk estimates of state variables and surface wind stress as per Equations 1 and 2:

$$Q_L = \rho L_e C_E U_r \Delta q \quad (1)$$

$$Q_S = \rho c_p C_H U_r \Delta \theta \quad (2)$$

where  $Q_L$  and  $Q_S$  are the surface latent and sensible heat fluxes, respectively,  $\rho$  is the density of air,  $L_e$  is the latent heat of vapourization,  $c_p$  is the specific heat capacity of air,  $C_E$  and  $C_H$  are empirically-derived transfer coefficients for latent and sensible heat, respectively,  $U_r$  is the scalar wind speed relative to the surface current, and  $\Delta q$  and  $\Delta \theta$  are the air-sea specific humidity and potential temperature gradients, respectively. A scalar wind reflects wind speed averaged over iterative time steps as per Equation 3:

$$U = \frac{1}{n} \sum_{t=1}^n u_t = \frac{1}{n} \left( \sqrt{u_1^2 + v_1^2} + \sqrt{u_2^2 + v_2^2} + \dots + \sqrt{u_n^2 + v_n^2} \right) \quad (3)$$

where  $U$  is the mean scalar wind speed,  $u$  and  $v$  are the zonal and meridional velocities, respectively,  $n$  is the total number of time steps within the averaging window, and  $t$  is an individual time step. Unfortunately, given the limited availability of wind measurements over the ocean, it is not always possible to resolve the scalar wind (depending on the averaging interval), and a vector wind must be used. A vector wind reflects an average of the horizontal wind components, meaning it is calculated based on time-averaged velocities as per Equation 4:

$$|\bar{u}| = \sqrt{\bar{u}^2 + \bar{v}^2} \quad (4)$$

where  $|\bar{u}|$  is the amplitude of the mean wind vector and the overbar represents a time average. Hence, while a 1-hr scalar wind is derived from instantaneous wind speed measurements over an hour, a vector wind is derived from hourly-averaged velocity measurements.

The Coupled Ocean-Atmosphere Response Experiment (COARE) 3.5 bulk flux algorithm (Edson et al., 2013; Fairall et al., 1996, 2003) relates near-surface atmospheric and oceanographic bulk variables through Monin-Obukhov similarity theory and parameterizations of roughness lengths and profile stability functions to estimate surface fluxes of momentum, sensible heat, and latent heat. Inputs to the COARE algorithm involve state variables collected from numerical or observational data, including 1-hr vector wind measurements.

However, within certain environments, such as tropical ocean regions with high solar insolation and weak surface winds, the amplitude of the mean wind vector does not properly represent the mean scalar wind speed (Cronin et al., 2006; Fairall et al., 1996; Godfrey & Beljaars, 1991). In other words, the mean wind vector fails to capture high-frequency wind variations within the averaging interval, and, if left uncorrected, can lead to significant errors in the estimate of bulk air-sea heat fluxes (Esbensen & McPhaden, 1996). To address this issue, the COARE 3.5 algorithm applies a “gustiness” parameter,  $u_g$ , that relates the scalar- and vector-averaged winds through the following equation:

$$u_g^2 = U^2 - |\bar{\mathbf{u}}|^2 \quad (5)$$

where  $u_g^2$  reflects the missing wind variance over a select time period. However, given a lack of high-resolution wind observations over vast ocean regions, the gustiness parameter,  $u_g$ , used in the COARE 3.5 algorithm (cf., Equation 8 in Fairall et al. (2003)) is tuned to hourly average values that accounts for the underestimation of air-sea fluxes associated with boundary layer large eddies within low-wind regimes during fair weather conditions (Edson et al., 2013; Fairall et al., 1996, 2003). Unfortunately, the gustiness estimate still struggles to resolve missing wind variance associated with convective precipitation and related phenomena on high-frequency, meso-gamma (5–20 km) scales (Cronin et al., 2006; Kilpatrick & Xie, 2015; Williams, 2001). Furthermore, with limited availability of high-resolution air-sea flux measurements, it is challenging to validate the bulk estimates against observations, making it difficult to evaluate the utility of the gustiness parameter in resolving air-sea heat fluxes (Serra, 2018).

Recent high-resolution data collected by novel Saildrone uncrewed surface vehicles (USV) in the eastern tropical Pacific provides new insight on variations in air-sea heat fluxes during convective cold pool events. Saildrone USVs are remotely-piloted drones capable of long-term deployment to observationally-sparse ocean regions that rely on solar power and wind energy to collect a suite of near-surface oceanic, atmospheric, and biogeochemical measurements (Zhang et al., 2019). As shown in Wills et al. (2021), Saildrone observations collected during three previous missions to the eastern tropical Pacific revealed high-frequency variations in wind, temperature, and humidity associated with atmospheric cold pool fronts over the ocean. Here, we utilize the high-resolution Saildrone data to evaluate the competing contributions of wind, temperature, and humidity in the calculation of bulk air-sea heat fluxes during convective cold pool events.

This study aims to address the importance of resolving sub-grid scale variability associated with mesoscale and smaller air-sea phenomena in the estimation of surface turbulent heat fluxes on sub-daily time scales. The remainder of the paper is organized as follows. Section 2 describes the observational data sets and satellite products used in the analysis, and Section 3 summarizes the methodology for identifying convective cold pool events. Section 4 examines composite time series results of bulk air-sea heat fluxes associated with convective cold pools and provides an assessment of the relative contributions from individual terms. Section 5 presents a cold pool case study and explores the implications of using vector and scalar wind averages in the estimation of bulk air-sea heat fluxes. A discussion and concluding remarks are provided in Section 6.

## 2. Data

### 2.1. In Situ Observing Platforms

This study utilizes high-resolution 1-min measurements of near-surface air (2.2 m) and sea surface temperature (SST; −0.6 m), humidity (2.2 m), wind (5 m), air pressure (0.3 m), and Acoustic Doppler Current Profiler (ADCP; −0.3 m)-derived ocean current velocities collected during three past Tropical Pacific Observing System (TPOS) Saildrone missions to the central (0°, 140°W) and eastern (0°, 125°W) tropical Pacific between 2017 and 2019 (Wills et al., 2021; Zhang et al., 2019). The measurements collected on each Saildrone are motion-corrected, and sensor heights are relative to the water line. Given that the drones were not equipped to directly measure air-sea fluxes, bulk surface heat flux and wind stress estimates are based on COARE 3.5 algorithm output derived from 10-min average Saildrone observations (Edson et al., 2013). As the COARE algorithm is built on Monin-Obukhov similarity theory, the 10-min flux data is the highest available resolution possible because 1-min timescales are not reflective of a sufficient mixture of eddies within an environment. Therefore, both 1-min and 10-min averaged Saildrone data are used throughout the analysis. Additional information on the TPOS missions and Saildrone data

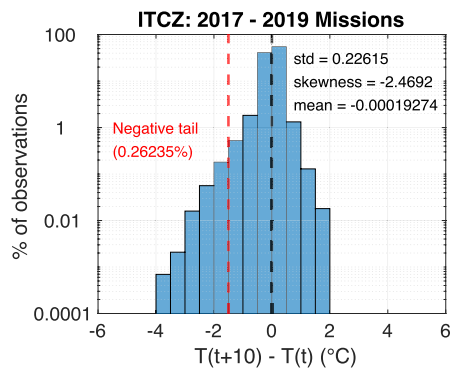


**Figure 1.** Histogram of 10-min air temperature ( $T$ ;  $^{\circ}\text{C}$ ) changes observed within the Intertropical Convergence Zone (bounded by the mean  $27.5^{\circ}\text{C}$  isotherm) by 10 Sairdron USVs from the 2017, 2018, and 2019 missions combined. Forward differencing is applied to 1-min air temperature time series to calculate the magnitude of change over 10-min windows across the full data record. Dashed black and red lines indicate threshold changes of  $0^{\circ}\text{C}$  and  $-1.5^{\circ}\text{C}$  over a 10-min window, respectively. Note that the data are plotted on a semi-log scale to emphasize the tails of the distribution.

is detailed in Wills et al. (2021), and the real-time telemetered 1-min data is publicly accessible through NOAA PMEL [<https://www.pmel.noaa.gov/ocs/sairdron/data-access>].

We also obtain 10-min resolution measurements of air temperature, wind speed, and zonal and meridional velocities from the Tropical Atmosphere Ocean (TAO) array maintained by NOAA's National Data Buoy Center (NDBC). The TAO array is a network of moored buoys deployed throughout the Tropical Pacific, spaced  $10^{\circ}$ – $15^{\circ}$  zonally between  $165^{\circ}\text{E}$  –  $95^{\circ}\text{W}$  and  $2^{\circ}$ – $4^{\circ}$  meridionally between  $8^{\circ}\text{S}$  and  $9^{\circ}\text{N}$  (McPhaden et al., 1998, 2010). The 10-min data is collected for the TAO buoy at  $9^{\circ}\text{N}$ ,  $140^{\circ}\text{W}$  for comparison in a cold pool case study on 17 November 2019 and is available at <https://www.pmel.noaa.gov/tao/drupal/disdel/>.

## 2.2. Gridded Reanalysis and Satellite Products

High-resolution precipitation estimates are obtained from the NASA Global Precipitation Measurement (GPM) gridded precipitation product, Integrated Multi-SatellitE Retrievals for GPM (IMERG) version 6b algorithm that is accessible at <https://doi.org/10.5067/GPM/IMERG/3B-HH/06> (Huffman et al., 2015). The IMERG calibrated precipitation product is available on a  $0.1^{\circ}$  horizontal grid with global spatial coverage and half-hourly temporal

sampling (Huffman et al., 2019). Given that rainfall is not a standard measurement on the Sairdron USV platforms, the gridded precipitation estimates are used to validate the presence of rainfall during a cold pool event detected near  $9^{\circ}\text{N}$ ,  $140^{\circ}\text{W}$  on 17 November 2019.

Near-surface (10-m) zonal ( $u$ ) and meridional ( $v$ ) wind velocities from the ECMWF ERA5 Reanalysis are used in comparison against high-resolution Sairdron wind measurements in Section 5. The ERA5 product is available on a  $0.25^{\circ}$  horizontal grid and provides hourly resolution reanalysis data defined as instantaneous values valid at the hour (Hersbach et al., 2018, 2020). Near-surface wind velocities from the  $0.5^{\circ}$  resolution NCEP Climate Forecast System version 2 (CFSv2) hourly time series analysis are also used for comparison in a Supporting Figure (Saha & Coauthors, 2014; Saha et al., 2011).

## 3. Classifying Convective Cold Pools

Atmospheric cold pool events are identified through raw 1-min air temperature time series per the criteria detailed in Wills et al. (2021), where an event is defined as a minimum temperature drop of  $-1.5^{\circ}\text{C}$  over a 10-min window. Given that the USVs collect measurements along a trajectory, the identifying criteria detects the passage of the leading edge of the cold air dome, signaling that the drone has entered into a local cold pool environment. Individual cold pool passages are restricted to occur at least 1 hr apart, meaning that subsequent temperature drops meeting the criteria within a 60-min window are disregarded. As noted in Wills et al. (2021), the majority of identified cold pool events occur within the Intertropical Convergence Zone (ITCZ), located within the bounds of the mean  $27.5^{\circ}\text{C}$  isotherm during the September - December season. Here we limit the analyses to only explore events within this ITCZ-band (i.e., in regions north of the equator with SST  $>27.5^{\circ}\text{C}$  for September-December) in an effort to isolate convective cold pools in known regions of heavily precipitating clouds.

Figure 1 highlights 10-min changes in air temperature observed by all 10 drones within the confines of the ITCZ for the 2017–2019 missions combined. Due to the large volume of data from the observational record, the histogram results are plotted on a semi-log scale to highlight the tails of the distribution. While the majority of observations indicate near-zero temperature changes over a 10-min window, there is a clear skew toward the negative tail of the distribution, with changes as large as  $-4^{\circ}\text{C}$  (in contrast to  $+2^{\circ}\text{C}$  in the positive tail). The minimum defining criteria for atmospheric cold pools used in this study (i.e.,  $-1.5^{\circ}\text{C}$  in 10 min, as indicated by dashed red line) falls within the extreme negative tail of the distribution, roughly six standard deviations from the mean. Despite accounting for less than 1% of the observational record, the extreme negative tail (i.e., the area to the left of the dashed red line) reflects a total of 378 qualifying 10-min air temperature drops, 276 of which are considered individual cold pool events occurring at least an hour apart on a single drone.

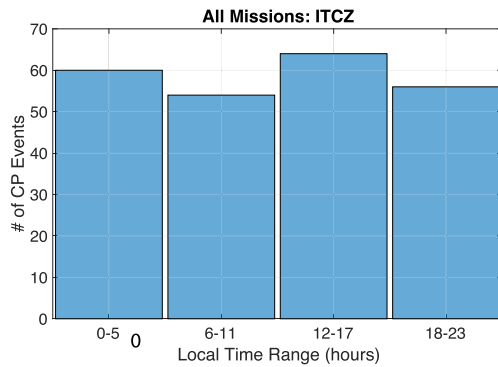


**Figure 2.** Histogram showing the local time of day of 234 sampled cold pool events from the 2017, 2018, and 2019 Tropical Pacific Observing System Missions. The results are adjusted to account for independent events and reflect the total number of cold pools sampled over the Intertropical Convergence Zone domain defined in the text. The timing of observed events is adjusted to local time based on longitude, rounded to the nearest hour, and organized into 6-hr bins over a 24-hr period.

Temperature criteria has often been used to identify atmospheric cold pool signatures in both observational data (Chandra et al., 2018; Chuda et al., 2008; de Szoeke et al., 2017; Garg et al., 2020, 2021; Kilpatrick & Xie, 2015; Terai & Wood, 2013; Zuidema et al., 2017) and model output (Drager & van den Heever, 2017; Feng et al., 2015; Grant & van den Heever, 2016; Gentine et al., 2016; Tompkins, 2001; Torri et al., 2015). Buoy observations are commonly used to identify cold pool signatures, with air temperature criteria ranging from  $-1.5^{\circ}\text{C}$  in 1 hr to  $-2^{\circ}\text{C}$  in 2 hr (Chandra et al., 2018; de Szoeke et al., 2017; Garg et al., 2020, 2021; Kilpatrick & Xie, 2015; Zuidema et al., 2017). Similarly, Chuda et al. (2008) used 1-min resolution shipboard measurements to identify strong atmospheric cold pools based on air temperature criteria of  $-3^{\circ}\text{C}$  in 30 min, with an additional constraint on temperature variability preceding the event. Given that previous ship-saildrone-buoy comparisons indicate good agreement between platforms and sensors (Zhang et al., 2019), we also utilize air temperature criteria (i.e.,  $-1.5^{\circ}\text{C}$  in 10 min) to isolate convective cold pools in high-resolution Saildrone USV data. It is important to note that this strict identifying criteria (here and in previous studies) likely misses cold pools at different stages of evolution, such as nascent or dissipating cold pools with very weak ( $<1^{\circ}\text{C}$ ) temperature deficits, and it is unclear if qualifying events originated from an initial convective

cell or the intersection of multiple existing cold pools. However, the application of a  $-1.5^{\circ}\text{C}$  threshold on the TPOS Saildrone observations selected events with better coherent variability of air temperature, relative humidity, and wind than that of  $-1^{\circ}\text{C}$ . Nevertheless, the results in this study remain robust for both weaker and stronger temperature thresholds (not shown).

To better understand the type of parent convection associated with and/or leading to intense cold pool fronts within the eastern Pacific ITCZ, we examine the local time (LT) of day when the extreme air temperature drop was recorded. The histogram in Figure 2 reflects the average number of cold pools sampled throughout the domain bounded by the mean  $27.5^{\circ}\text{C}$  isotherm ( $\sim 2^{\circ}\text{N}$ – $18^{\circ}\text{N}$ ). The events are organized into four 6-hr bins over a 24-hr period, with time windows spanning 00:00–05:00 LT, 06:00–11:00 LT, 12:00–17:00 LT, and 18:00–23:00 LT. Given that the drones often sailed in close proximity during each mission, the 276 individual cold pool observations likely reflect instances where multiple drones sampled the same event from different positions. While we treat cold pool measurements from each drone as *independent observations* in composite analyses (see Section 3), we must account for *independent events* to properly resolve the diurnal cycle. To do this, we consider “duplicate” events between drones if the timing of the temperature drop is within a  $\pm 60$ -min window and the drones are less than 100 km apart. If “duplicate” events are detected between two or more drones, only one is counted as an *independent event* for evaluating the diurnal cycle. Hence, the results in Figure 2 are based on a total of 234 independent events.

The atmospheric cold pool passages identified in this study occur throughout the diurnal cycle, with a slight preference for the mid- to late-afternoon hours based on the results in Figure 2. Generally, maximum precipitation over ocean regions tends to occur in the late-night to early-morning hours due to radiative cooling, which acts to destabilize the boundary layer by lowering the air temperature relative to the ocean surface (Bowman et al., 2005; Dai, 2001; Gray & Jacobson, 1977; Serra & McPhaden, 2004). However, recent studies have also shown a secondary signal in afternoon precipitation over the tropical ocean associated with convective cells in the early stages of development (Brilouet et al., 2021; de Szoeke et al., 2021; Garg et al., 2021; Serra & McPhaden, 2004). Using rain gauge measurements on moored buoys across the tropical oceans, Serra and McPhaden (2004) identified differing diurnal cycles in rain accumulation and the contributing components of rain intensity and frequency. In their findings, the secondary peak in afternoon rain accumulation is associated with a secondary maximum in afternoon (i.e., 13:00–15:00 LT) rain intensity, a signal which is especially prominent in the northeast Pacific ITCZ between June–November. In contrast, the authors found a single early morning (i.e., 03:00–06:00 LT) peak in rain frequency, when stratiform rain is at its maximum. A similar afternoon peak was observed in buoy identified cold pools and gust fronts in the eastern Pacific basin by Garg et al. (2021), who argue that the timing is likely associated with scattered and/or immature cells early in the convective life cycle that are not easily detected in satellite-derived wind products. Indeed, similar to the findings of Simpson (1969),

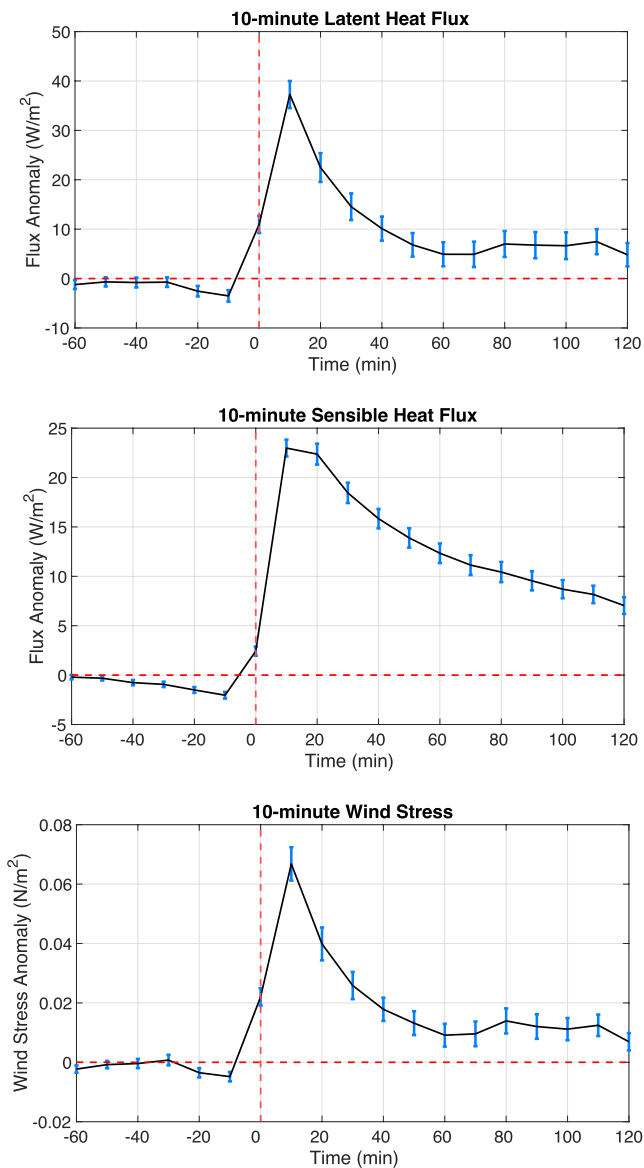


**Figure 3.** Ensemble-mean composite time series of (a) 10-min latent heat flux ( $\text{W/m}^2$ ), (b) 10-min sensible heat flux ( $\text{W/m}^2$ ), and (c) 10-min wind stress ( $\text{N/m}^2$ ) associated with cold pool events detected during the 2017, 2018, and 2019 missions. Error bars are shown in blue and represent the standard error of the ensemble mean. Anomalies are calculated relative to the -2 hr mean field and represent departures from the environmental conditions prior to the cold pool passage (defined to begin at lag-0).

latent heat flux anomalies, with ensemble-mean values peaking up to  $0.06 \text{ N/m}^2$ . However, given that the fluxes are computed as 10-min averages, it is possible that the timing of peak magnitude occurs within minutes of the temperature front, as will be discussed in the following section. Prior to the cold pool passage, latent and sensible heat fluxes derived from Sairdrones USV measurements ranged between  $110\text{--}115 \text{ W/m}^2$  and  $5\text{--}10 \text{ W/m}^2$ , respectively (not shown). Considering the background environmental conditions, the anomalous turbulent heat fluxes associated with the cold pool front resulted in total latent and sensible heat fluxes peaking near  $150 \text{ W/m}^2$  and  $33 \text{ W/m}^2$ , respectively.

The results in Figure 3 reveal high frequency variations in surface air-sea heat fluxes associated with convective cold pools over the tropical ocean. Previous studies on the eastern Pacific ITCZ report long-term mean

Schiro and Neelin (2018) found a link between the strength of convective events and near-surface temperature depressions, suggesting that downdrafts associated with stronger rain intensities yield larger temperature drops at the surface. Based on this evidence, we assume that the identification criteria in our study isolates convective cold pools generated by convective-scale downdrafts on meso-gamma scales associated with intensely-precipitating organized and unorganized cells throughout the diurnal cycle.

## 4. Composite Results

### 4.1. Convective Cold Pools and Bulk Flux Estimates

As shown in the previous section, convective cold pools identified in this study are associated with high-frequency changes in air temperature of at least  $-1.5^\circ\text{C}$  over a 10-min window throughout the eastern tropical Pacific ITCZ region. Wills et al. (2021) demonstrated that temperature fronts of this magnitude are associated with large variations in near-surface wind speed, in addition to smaller but significant variations in sea level pressure and humidity. Given their influence on state variables, convective cold pools are also capable of altering air-sea heat and momentum fluxes in the lower atmospheric boundary layer, albeit on local scales (Chuda et al., 2008; de Szoeke et al., 2017; Gentine et al., 2016; Grant & van den Heever, 2016; Tompkins, 2001; Young et al., 1995). In this section, we estimate the role of convective cold pools in altering the background environment and modulating air-sea fluxes over the ocean.

Figure 3 shows the ensemble-mean composite time series of bulk air-sea heat flux and wind stress estimates associated with 276 convective cold pool passages observed throughout the entire eastern Pacific ITCZ study region during the 2017–2019 TPOS missions combined (cf., Figure 1 in Wills et al. (2021) for drone track and cold pool locations). Similar to the analysis performed in Wills et al. (2021), the cold pool composites reflect anomalies relative to the -2 hr mean field leading the air temperature drop; in other words, the composite anomalies indicate departures from the background environment prior to the cold pool passage, which is defined to begin at lag-0 in conjunction with the timing of the observed air temperature drop. Hence, we argue that anomalies at positive lags represent local changes to the environment due to cold pool activity.

The ensemble-mean composite time series in Figures 3a and 3b indicate enhanced latent and sensible heat fluxes following behind the leading edge of the cold pool front, with positive values reflecting ocean to atmosphere transfer. The heat fluxes appear to peak approximately 10 min after the beginning of the temperature drop (defined as lag-0), with average latent and sensible heat fluxes increasing by  $36$  and  $23 \text{ W/m}^2$ , respectively. Interestingly, the wind stress anomalies in Figure 3c exhibit a similar pattern to that of the

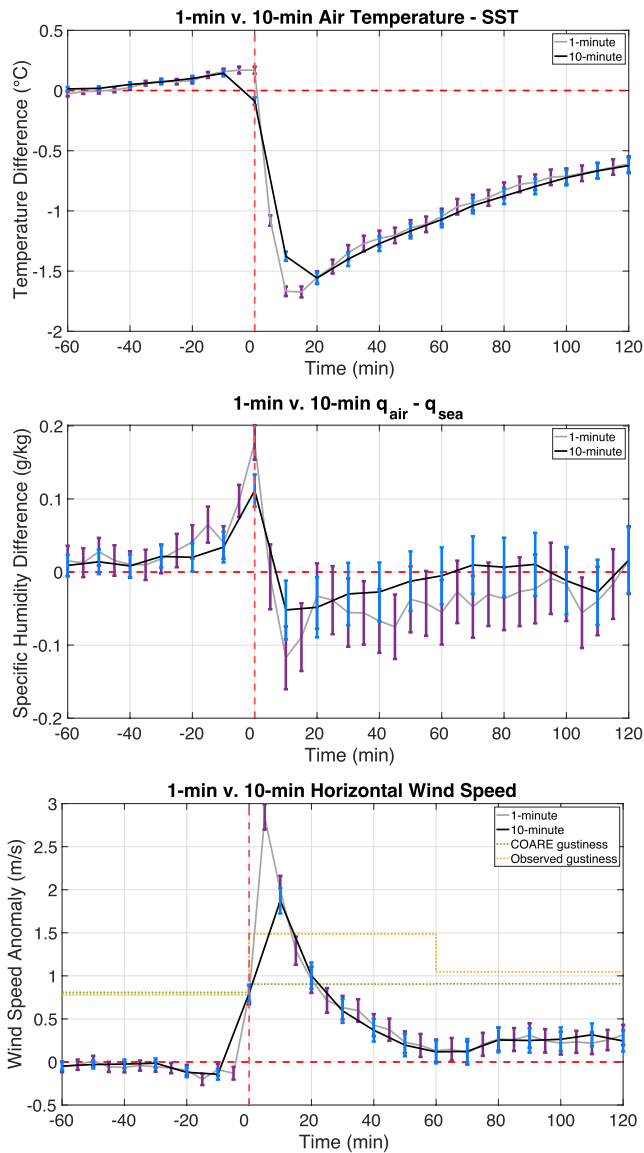


**Figure 4.** Same as in Figure 3, except for ensemble-mean composite time series of anomalous (a) air temperature - sea surface temperature ( $^{\circ}\text{C}$ ), (b) specific humidity - surface saturated specific humidity ( $\text{g/kg}$ ), and (c) wind speed ( $\text{m/s}$ ). Black (gray) lines represent 10-min averaged (1-min averaged) measurements, and error bars are shown in blue (purple).

temperature begins to drop. These discrepancies do not affect the interpretation of results presented here, *but* they do highlight the importance of high-resolution observations for resolving high-frequency phenomenon. Following the frontal passage, the anomalous air-sea temperature gradient is slow to recover within the cold air dome in both the 1-min and 10-min data, recovering a full degree roughly two hours after the event, or  $\sim 67\%$  of the temperature deficit. However, given the distribution of events throughout the diurnal cycle in Figure 2 and the continuous drone movement, the recovery statistics require further investigation beyond the scope of the current paper.

In contrast to the anomalous air-sea temperature gradient, the results in Figure 4b indicate an increase in the anomalous air-sea humidity gradient during the 20-min window prior to the cold pool passage, suggesting a brief surge in moisture associated with the leading edge of the frontal boundary (Langhans & Romps, 2015; Tompkins, 2001; Zuidema et al., 2017). Interestingly, the initial increase in the air-sea humidity gradient is

values ranging between  $100\text{--}200\text{ W/m}^2$  and  $5\text{--}25\text{ W/m}^2$  for latent and sensible heat fluxes, respectively, consistent with background environmental bulk flux estimates derived from high-resolution Saildrone USV measurements (Large & Yeager, 2009; Tomita et al., 2019). In terms of temporal variability, however, Wang and McPhaden (2000) report interannual variations in latent and sensible heat fluxes on the order of  $20\text{--}30\text{ W/m}^2$  and  $5\text{ W/m}^2$ , respectively. While the sub-daily variations in surface latent heat fluxes associated with cold pool events are of similar magnitude to variations on low-frequency time scales, the sub-daily variations in surface sensible heat fluxes are not. Instead, the results in Figure 3b suggest that variations in sensible heat fluxes are much larger on sub-daily, if not sub-hourly, time scales, highlighting the need to resolve high-frequency time scales of variability.

#### 4.2. Flux Decomposition

The results presented in the previous section indicate that convective cold pools observed during the 2017–2019 TPOS missions altered the local environment through increased surface sensible and latent heat fluxes and wind stress along the leading edge of the frontal boundary. However, it is not yet clear what physical processes are responsible for the increased ocean-to-atmosphere fluxes shown in Figure 3. Revisiting Equations 1 and 2, the key components modulating sensible and latent heat fluxes include scalar wind speed and air-sea specific humidity and temperature differences. Given the availability of high-resolution Saildrone USV measurements, Figure 4 highlights the ensemble-mean composite time series of each anomalous component, with results shown for both 10-min and 1-min averaged quantities. Due to constraints on battery life throughout the missions, sensor sampling schemes were sometimes adjusted to record 1-min measurements every 5 min, and therefore the ensemble-mean results reflect 1-min averages plotted at 5-min intervals. Note that the temperature and humidity gradients are calculated as atmosphere minus ocean to capture the cooling effect due to the local cold pool air mass, whereas the bulk heat flux estimates are calculated as ocean minus atmosphere per the COARE 3.5 algorithm (Edson et al., 2013).

The air-sea temperature differences shown in Figure 4a are consistent with the cold pool criteria detailed in Section 3, with the 1-min (gray line) and 10-min (black line) results indicating a rapid drop in air temperature compared to sea surface temperature of  $\sim -1.5^{\circ}\text{C}$  (but closer to  $-1.7^{\circ}\text{C}$  in the 1-min data). The stronger rate of change in the 1-min time series reveals a sensitivity to the averaging interval, likely because the timing of the temperature drop varies within a 10-min window (not shown). In other words, the 10-min averaging window blends the timing of events, muddying the exact time when the

coincident with increases in air temperature and horizontal wind speed as shown in Figures 4a and 4c, respectively. Considering a similar increase in sea level pressure found prior to the temperature front in Wills et al. (2021), this result likely reflect moisture convergence along the leading edge of the gust front boundary, possibly explaining the negative flux anomalies preceding the temperature front in Figure 3. The induced convergence is a dynamical effect of the cold pool itself, suggesting that the gust front begins prior to the temperature front, consistent with findings by van den Heever et al. (2021). After the initial surge, the anomalous moisture gradient drops rapidly, flipping sign to reflect the intrusion of drier air within the cold pool dome. The timing of results in Figure 4b is consistent between the 1-min and 10-min averaged data, with the latter displaying lower amplitude peaks. Similarly, the results in Figure 4c indicate that the 10-min averaged observations underestimate the magnitude of peak wind speeds by almost half, with 1-min and 10-min wind measurements reporting wind speed anomalies up to approximately 3 m/s and 1.5 m/s, respectively.

Considering that the heat fluxes in Figure 3 are derived from 10-min averages, the remainder of this section will focus on the 10-min averaged fields presented in Figure 4 to explore the relative roles of wind, temperature, and humidity in modulating surface air-sea fluxes during cold pool events. To better understand the competing contributions of state variables to the anomalous surface heat fluxes shown in Figure 3, we expand Equations 1 and 2 into the following forms:

$$Q_L = \rho_a L_e C_E (\overline{U_r} + U_r') [(\overline{q_s} + q_s') - (\overline{q_a} + q_a')] \quad (6)$$

$$Q_S = \rho_a c_p C_H (\overline{U_r} + U_r') [(\overline{\theta_s} + \theta_s') - (\overline{\theta_a} + \theta_a')] \quad (7)$$

where overbars represent the composite -2 hr mean field (i.e., pre-cold pool passage conditions), primes represent the composite deviation at each time step from the -2 hr mean field (i.e., post-cold pool passage conditions),  $\theta_a'$ / $\theta_s'$  represent the atmosphere/sea surface temperature, respectively, and  $q_a'$ / $q_s'$  represent the atmosphere/sea surface specific humidity, respectively. Based on these definitions, and following the methodologies of Yang et al. (2016), Chuda et al. (2008), and Tanimoto et al. (2003), we make the following assumptions:

1. Between -120 and 0 min (i.e., pre-cold pool),  $X = \overline{X}$
2. After lag-0 (i.e., post-cold pool),  $X = \overline{X} + X'$

where  $X$  can be substituted for  $Q_L$  or  $Q_S$ . Given that perturbations are assumed negligible during pre-cold pool conditions, we define the mean latent and sensible heat fluxes as:

$$\overline{Q_L} = \rho_a L_e C_E \left[ \overline{U_r} (\overline{q_s} - \overline{q_a}) \right] \quad (8)$$

$$\overline{Q_S} = \rho_a c_p C_H \left[ \overline{U_r} (\overline{\theta_s} - \overline{\theta_a}) \right] \quad (9)$$

Subtracting Equations 8 and 9 from Equations 6 and 7, respectively, and expanding terms, we solve for the anomalous latent and sensible heat fluxes during post-cold pool conditions as follows:

$$Q'_L = \rho_a L_e C_E \left[ \overline{U_r} \overline{q_s} + U_r' \overline{q_s} + \overline{U_r} q_s' + U_r' q_s' - \overline{U_r} \overline{q_a} - U_r' \overline{q_a} - \overline{U_r} q_a' - U_r' q_a' - \overline{U_r} \overline{q_s} + \overline{U_r} \overline{q_a} \right] \quad (10)$$

$$Q'_S = \rho_a c_p C_H \left[ \overline{U_r} \overline{\theta_s} + U_r' \overline{\theta_s} + \overline{U_r} \theta_s' + U_r' \theta_s' - \overline{U_r} \overline{\theta_a} - U_r' \overline{\theta_a} - \overline{U_r} \theta_a' - U_r' \theta_a' - \overline{U_r} \overline{\theta_s} + \overline{U_r} \overline{\theta_a} \right] \quad (11)$$

Simplifying the terms and rearranging the right-hand side (RHS) of Equations 10 and 11, we are left with the following key terms:

$$Q'_L = \rho_a L_e C_E \left[ \overline{U_r} (q_s' - q_a') + U_r' (\overline{q_s} - \overline{q_a}) + U_r' (q_s' - q_a') \right] \quad (12)$$

$$Q'_S = \rho_a c_p C_H \left[ \overline{U_r} (\theta_s' - \theta_a') + U_r' (\overline{\theta_s} - \overline{\theta_a}) + U_r' (\theta_s' - \theta_a') \right] \quad (13)$$

where the first term on the RHS of Equations 12 and 13 reflects the mean background wind acting on the anomalous air-sea gradient, the second term reflects the anomalous wind speed acting on the mean background air-sea



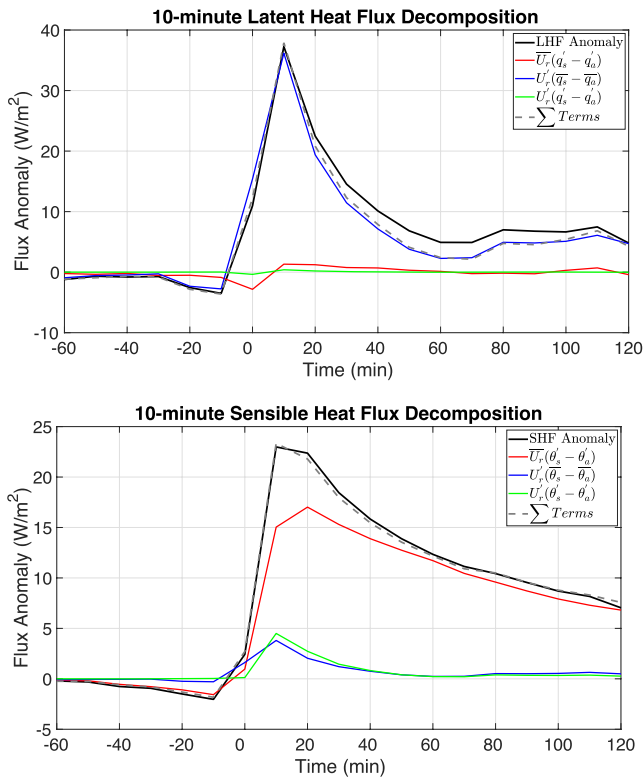


**Figure 5.** Ensemble-mean composite time series of 10-min (a) latent heat flux ( $\text{W/m}^2$ ) and (b) sensible heat flux ( $\text{W/m}^2$ ) anomalies and contributing terms. Positive fluxes indicate ocean-to-atmosphere transfer.

gradient, and the third term reflects the anomalous wind speed acting on the anomalous air-sea gradient.

Given the available Saildrone USV observations, we are able to calculate the individual terms on the RHS of Equations 12 and 13 to evaluate the key processes contributing to anomalous air-sea heat fluxes during convective cold pool events. Similar to Figures 3a and 3b, Figure 5 highlights the ensemble-mean surface latent and sensible heat flux anomalies associated with cold pool events, but with the individual terms on the RHS of Equations 12 and 13 also included. The summation of terms (dashed lines) indicate good agreement between the decomposition and observed heat fluxes estimates, with a slight underestimation of surface heat fluxes in the 2-hr window following the cold pool passage. We suspect that the slight underestimation in both sensible and latent heat fluxes is due to the use of constant values for the  $C_h$  and  $C_e$  transfer coefficients of 0.00145 and 0.0015, respectively, which have been shown to vary with wind speed (Fairall et al., 1996, 2003). Additionally, due to bad sensor readings, a constant salinity value of 35 PSU is used to calculate the surface saturated specific humidity, limiting the representation of freshwater lenses due to rainfall following a cold pool passage.

Nevertheless, the results in Figure 5 reveal key insights into the dominant terms and physical processes regulating surface latent and sensible heat fluxes during cold pool events. According to the results in Figure 5a, the second term on the RHS of Equation 12 ( $U'_r(\bar{q}_s - \bar{q}_a)$ ) provides the largest contribution to the observed latent heat flux anomalies, highlighting the relative importance of the anomalous wind field acting on the mean background air-sea moisture gradient. In other words, increased wind speeds associated with the cold pool gust front apply a mechanical forcing along the air-sea interface to enhance moisture fluxes from the ocean to the atmosphere. Similar findings were reported by Chuda et al. (2008) and Saxen and Rutledge (1998), who studied the influence of precipitating clouds on turbulent heat fluxes in the western tropical Pacific. But different findings were reported in a recent study by Simoes-Sousa et al. (2023), who evaluated the impact of cold pools on turbulent heat fluxes near 18°N in the Bay of Bengal. In their study, it was found that the anomalous air-sea moisture gradient plays a dominant role in enhancing latent heat fluxes compared to anomalous winds during cold pool events; however, the authors note that this result may be due to the decreasing contribution of wind with increasing latitude, as found by Joseph et al. (2021).

In contrast to the latent heat flux terms, Figure 5b indicates that the first term on the RHS of Equation 13 ( $\bar{U}_r(\theta'_s - \theta'_a)$ ) provides the largest contribution to the observed sensible heat flux anomalies, highlighting the importance of the mean background wind field acting on the anomalous air-sea temperature gradient. This result suggests that temperature changes associated with the cold pool air mass apply a thermodynamic forcing at the surface to enhance the exchange of heat from the ocean to the atmosphere. The results in Figure 5b further indicate contributions (albeit smaller) from the second ( $U'_r(\bar{\theta}_s - \bar{\theta}_a)$ ) and third ( $U'_r(\theta'_s - \theta'_a)$ ) terms on the RHS of Equation 13, indicating the non-negligible impact of enhanced wind speeds on sensible heat fluxes. In fact, while our results generally agree with those of Simoes-Sousa et al. (2023), Chuda et al. (2008), and Saxen and Rutledge (1998), Chuda et al. (2008) found the third term on the RHS of Equation 13 to be the dominant contributor to sensible heat fluxes over the western tropical Pacific. The discrepancy in contributing terms between our study and those of Chuda et al. (2008) are likely due to both stricter identifying criteria and different environmental regimes that characterize the eastern tropical Pacific v. western tropical Pacific. For example, Chuda et al. (2008) observed mean background wind speeds of 2.6 m/s prior to convective events in the western basin, while our observations in the eastern basin indicated mean background wind speeds of 6.2 m/s prior to cold pool passages (not shown). Furthermore, for cold pools identified by a criteria of  $-3^\circ\text{C}$  in 30 min, Chuda et al. (2008) observed peak wind speed anomalies of approximately 10 m/s, while our ensemble-mean results indicate peak wind speed anomalies of 1.5 m/s or 3 m/s, depending on the averaging interval. Hence, consistent with the latent heat flux findings in Simoes-Sousa et al. (2023), it would appear the impact of cold pools on surface turbulent heat fluxes varies across tropical ocean regions.

The decomposition results in Figure 5 have important implications for calculating bulk flux estimates along the air-sea interface. First, our results indicate the sensitivity of latent heat flux estimates (and to a lesser extent sensible heat flux estimates) to wind speed anomalies during convective cold pool conditions. Previous studies report similar findings on the need to resolve high-frequency wind variability within stable, low-wind regimes, emphasizing the role of scalar wind in calculating bulk air-sea heat fluxes (Cronin et al., 2006; Esbensen & McPhaden, 1996; Fairall et al., 1996; Godfrey & Beljaars, 1991). Indeed, the 10-min averaged wind speed anomalies in Figure 4c display a reduction in peak amplitude of almost half compared to the 1-min composite wind speed results, highlighting the need for a gustiness parameter in the COARE 3.5 algorithm to capture missing wind speed variance due to the averaging (or sampling) interval (Edson et al., 2013; Fairall et al., 2003). Second, our results further indicate that sensible heat flux estimates are more sensitive to temperature variations compared to wind speed variations (at least in the eastern tropical Pacific regime) during convective cold pool conditions. In the next section, we present a cold pool case study evaluating the smaller spatial and temporal scales of variability captured by Saildrone USV observations in comparison against COARE 3.5 output.

## 5. Convective Cold Pool Case Study

### 5.1. Saildrone USVs as a Traveling Mesonet

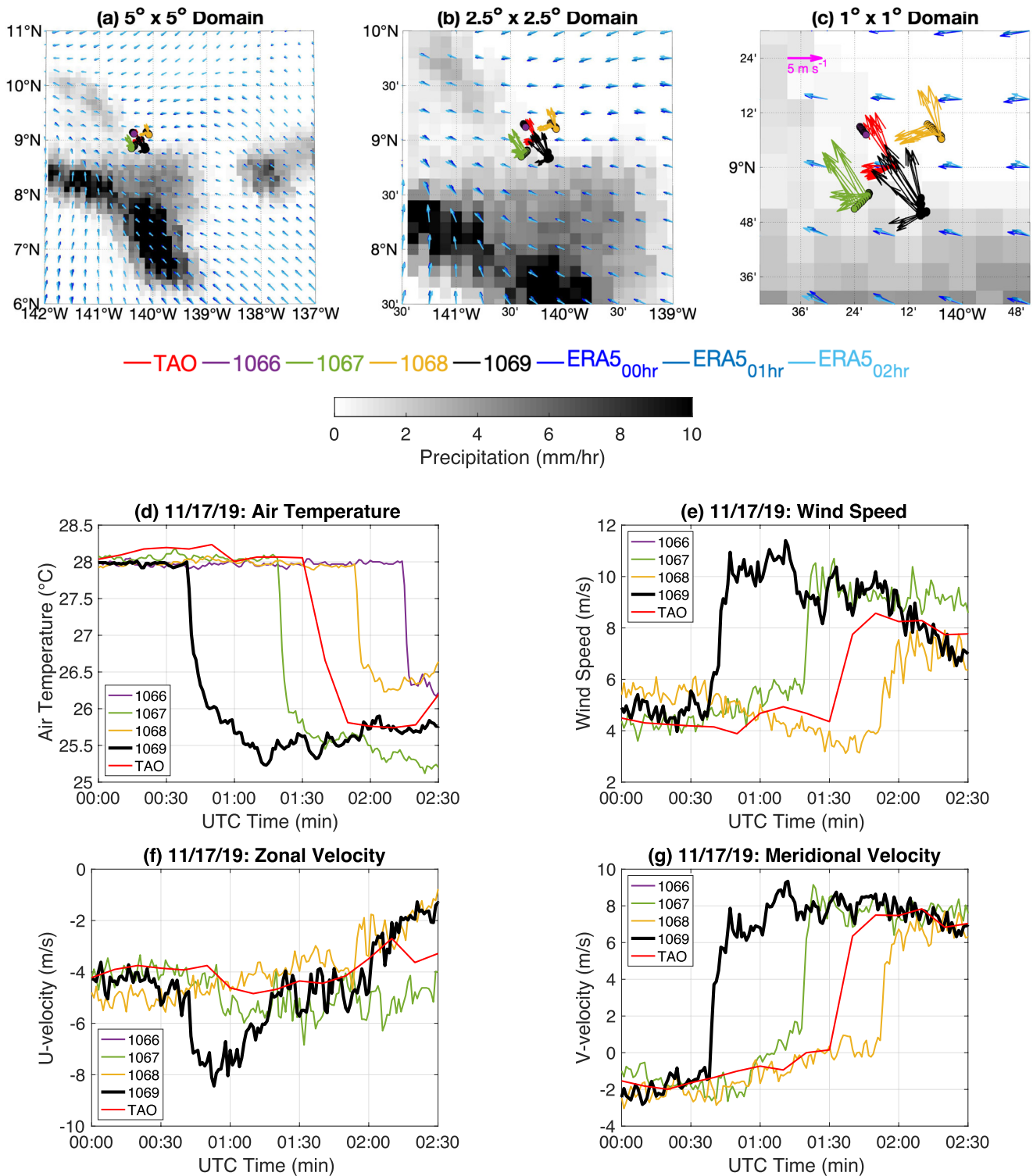
The ensemble-mean composite results presented in the previous section suggest that higher temporal resolution observations, such as those collected by Saildrone USVs, are needed to properly resolve convective cold pool activity over the eastern tropical Pacific. However, in addition to the temporal sampling, USVs offer increased spatial coverage as they operate on a space-time continuum. Not only are the drones able to travel far distances over remote ocean regions, but when operating in a group of two or more, they are able to form a traveling “mesonet”, or mesoscale network, to sample time and space scales simultaneously (Brock et al., 1995; Engerer et al., 2008; Wills et al., 2021). For the safety of the vehicles, the drones maintain a minimum separation of 5 km when transiting the ocean, but this distance is marginal compared to the nominal spacing of the TAO array, with distances between buoys ranging hundreds and thousands of kilometers across latitude and longitude, respectively (McPhaden et al., 1998, 2010). Therefore, for localized air-sea phenomena such as atmospheric cold pools, a traveling mesonet comprised of USVs is able to “fill in the gaps” of the buoy network and observe smaller scales of air-sea variability in both time and space.

Figure 6 details a case study on 11 November 2019, when four USVs formed a traveling mesonet about the 9°N, 140°W TAO mooring to observe cold pool activity within the northern hemisphere ITCZ. To create the mesonet, the drones were staged in the corners of a ~30 km box centered about the mooring, holding position while sailing 10 km butterfly formations (not shown). Figures 6a–6c show the locations of the observing platforms (depicted by purple, green, red, yellow, and black shaded circles) within 5°, 2.5°, and 1° grid domains, demonstrating how the mesonet configuration can be used to capture sub-grid variability on smaller spatial scales. For reference, gridded IMERG precipitation (gray shading) and ERA5 reanalysis winds (blue shaded vectors) are plotted at 0.1° and 0.25° horizontal resolution, respectively. Additionally, coarser gridded NCEP CFSv2 hourly winds are plotted at 0.5° horizontal resolution in Figure S1.

A cold pool front was detected during the time window 00:00–02:30 UTC by all four drones and the TAO mooring, with drone 1069 the first to record the air temperature drop in the southeast corner of the mesonet. While the drones are not equipped to measure rainfall, satellite retrievals valid at 00:30 UTC (Figures 6a–6c, gray shading) reveal a band of precipitation to the south of the mesonet, 10 min before drone 1069 encountered the air temperature front (Figure 6d). Additionally, the platform measurements recorded a shift in wind direction immediately following the temperature drop at each individual location, transitioning from an east-northeasterly flow to a south-southeasterly flow (Figures 6a–6c, green, red, yellow, and black vectors). In contrast, hourly resolution reanalysis winds (Figures 6a–6c, blue vectors) between 00:00–02:00 UTC indicate large-scale easterly flow throughout the domain. Note that wind measurements were not available on drone 1066 (purple shading) due to a sensor malfunction.

High-resolution time series of temperature and wind in Figures 6d–6g provide a more detailed understanding of the cold pool evolution across the mesonet. During this time period, 1-min averages were recorded every minute. A synopsis of the results is as follows, in order of frontal passage (all times in UTC):

- *SE corner* (8.8383°N, 140.1413°W): SD1069 observes a temperature front beginning at 00:39, dropping  $-2^{\circ}\text{C}$  by 00:49. Wind speed rises simultaneously, increasing  $\sim 5\text{ ms}^{-1}$  by 00:47.
- *SW corner* (8.8993°N, 140.3513°W): SD1067 observes a temperature front beginning at 01:19, dropping  $-2.1^{\circ}\text{C}$  by 01:24. Wind speed begins to rise at 01:20, increasing  $\sim 5\text{ ms}^{-1}$  by 01:24.



**Figure 6.** An atmospheric cold pool event detected on 11/17/19 between 00:00–02:30 UTC near 9°N, 140°W. Panels (a–c) depict different grid domains with half-hourly precipitation estimates (gray shading; mm/hr) valid 11/17/19 00:30 UTC and hourly 10-m u,v winds (blue vector shades; m/s) valid 11/17/19 00:00–02:00 UTC. Shaded circles represent the positions of the four Sairdrone USVs and the 9°N, 140°W Tropical Atmosphere Ocean (TAO) mooring, and the corresponding shaded vectors represent the u,v winds observed every 10 min between 00:00–02:30 UTC on 11/17/19. The bottom four panels show the 1-min time series of (d) air temperature, (e) wind speed, (f) zonal velocity, and (g) meridional velocity measured by the Sairdrone USVs and TAO mooring between 00:00–02:30 UTC on 11/17/19. Note that wind measurements for SD1066 are unavailable for the time period.

- *Center* (9.005°N, 140.255°W): The TAO buoy observes a temperature front beginning around 01:30, dropping  $-1.4^{\circ}\text{C}$  and  $-2.2^{\circ}\text{C}$  by 01:40 and 01:50, respectively. Wind speed begins to rise at 01:40, increasing  $\sim 4\text{ ms}^{-1}$  by 01:50.
- *NE corner* (9.1165°N, 140.0801°W): SD1068 observes a temperature front beginning at 01:53, dropping  $-1.4^{\circ}\text{C}$  by 01:57. Wind speed rises simultaneously, increasing  $\sim 2\text{ ms}^{-1}$  by 02:00.
- *NW corner* (9.1234°N, 140.3594°W): SD1066 observes a temperature front beginning at 02:14, dropping  $-1.7^{\circ}\text{C}$  by 02:18. Wind speed information is not available.

While an in-depth analysis of the November 17 cold pool event is beyond the scope of the current paper, it is clear that the statistics afforded by the traveling mesonet provide critical information for resolving propagation speed and direction, cold pool lifespan, dissipation statistics, and more. However, it is important to note that these statistics are limited to the mesonet configuration (i.e., orientation, spacing, number of drones, etc.) and position of the cold pool center relative to the mesonet. For example, weaker drops in air temperature and smaller increases in wind speed observed along the northern edge of the mesonet suggest that the cold pool expansion is approaching its limit, likely marking a transition to the dissipation stage of its life cycle. Unfortunately, there are no in situ data points beyond the mesonet drones, thus limiting the type of information we can infer, such as the size of the cold pool or the circle of impact. Nevertheless, the traveling mesonet provides insight on other important physical relationships, such as that between the temperature front and wind speed; the results suggest that increases in wind speed scale with the strength of the temperature front, consistent with previous findings (Feng et al., 2015; Garg et al., 2020; Kilpatrick & Xie, 2015; Schiro & Neelin, 2018; Simpson, 1969). Aside from exploring physical relationships, the in situ information provided by the mesonet is also useful for validating satellite retrievals and reanalysis products.

## 5.2. Scalar v. Vector Winds

This section focuses on the high-frequency wind and temperature measurements collected on SD1069, denoted by the bold black time series in Figures 6d–6g. As summarized above, the cold pool temperature front observed by SD1069 is accompanied by an increase in wind speed, or the cold pool gust front. In addition to enhanced winds, the gust front is associated with a roughly  $90^{\circ}$  shift in wind direction compared to pre-frontal conditions, largely due to the sign reversal and increasing strength of the meridional wind component (Figure 6g). Given the availability of high-resolution wind observations, we utilize Equations 3 and 4 to calculate the hourly-average scalar and vector wind magnitudes, respectively, based on the 1-min zonal and meridional velocities (Figures 6f and 6g, thick black line) over the time window 00:00–01:00 UTC, during which SD1069 encounters the cold pool passage. We explore hourly timescales (in addition to 10-min timescales later in the section) as this is often the highest resolution available for coupled model output, and a key aspect of this research is to use Saildrone observations to quantify the degree of missing variance, particularly in the wind field. The results indicate that the hourly-average scalar and vector wind speeds are 6.3 m/s and 5.4 m/s, respectively. Importantly, the results reveal that the squared difference between the hourly-averaged scalar and vector wind (i.e., the 1-hr missing wind variance) is  $\sim 11\text{ m}^2/\text{s}^2$ , relating to a gustiness parameter of 3.3 m/s per Equation 5.

In addition to the 17 November 2019 cold pool event, Figure 7a provides a comparison of the 1-hr missing wind variance derived from 1-min USV observations (calculated per Equation 5; black lines) and hourly-average COARE 3.5 estimates (calculated as the square of the output gustiness parameter,  $u_g$ ; light blue lines) for the entire SD1069 mission record. In contrast to the USV direct measurements, the gustiness parameter in the COARE 3.5 algorithm is calculated as a function of the parameterized buoyancy flux, which is a measure of stability in the planetary boundary layer. For reference, the hourly time series is organized such that each consecutive increment begins at the top of the hour (i.e., 00:00–00:59, 01:00–01:59, etc.), with the corresponding latitude labeled in lieu of the timestamp. The results in Figure 7a reveal that the COARE 3.5 algorithm largely underestimates the 1-hr missing wind variance associated with the November 17 cold pool event during the time window 00:00–01:00 UTC (denoted by star marker), with a gustiness output of 0.84 m/s, or missing wind variance of  $0.7\text{ m}^2/\text{s}^2$  (compared to  $11\text{ m}^2/\text{s}^2$  from observations!). Similarly, the gustiness parameter appears to underestimate the missing wind variance during other 1-hr windows with convective cold pool occurrences (denoted by pink circles), likely due to high-frequency variations in wind speed and direction not captured by the vector wind, as demonstrated in the Figure 6 case study. This result is further highlighted in Figure 4c, which includes the ensemble-mean composite gustiness from COARE output (green dotted line) and USV observations (orange dotted line) in front-relative coordinates for the hours before, during, and after the cold pool passage.

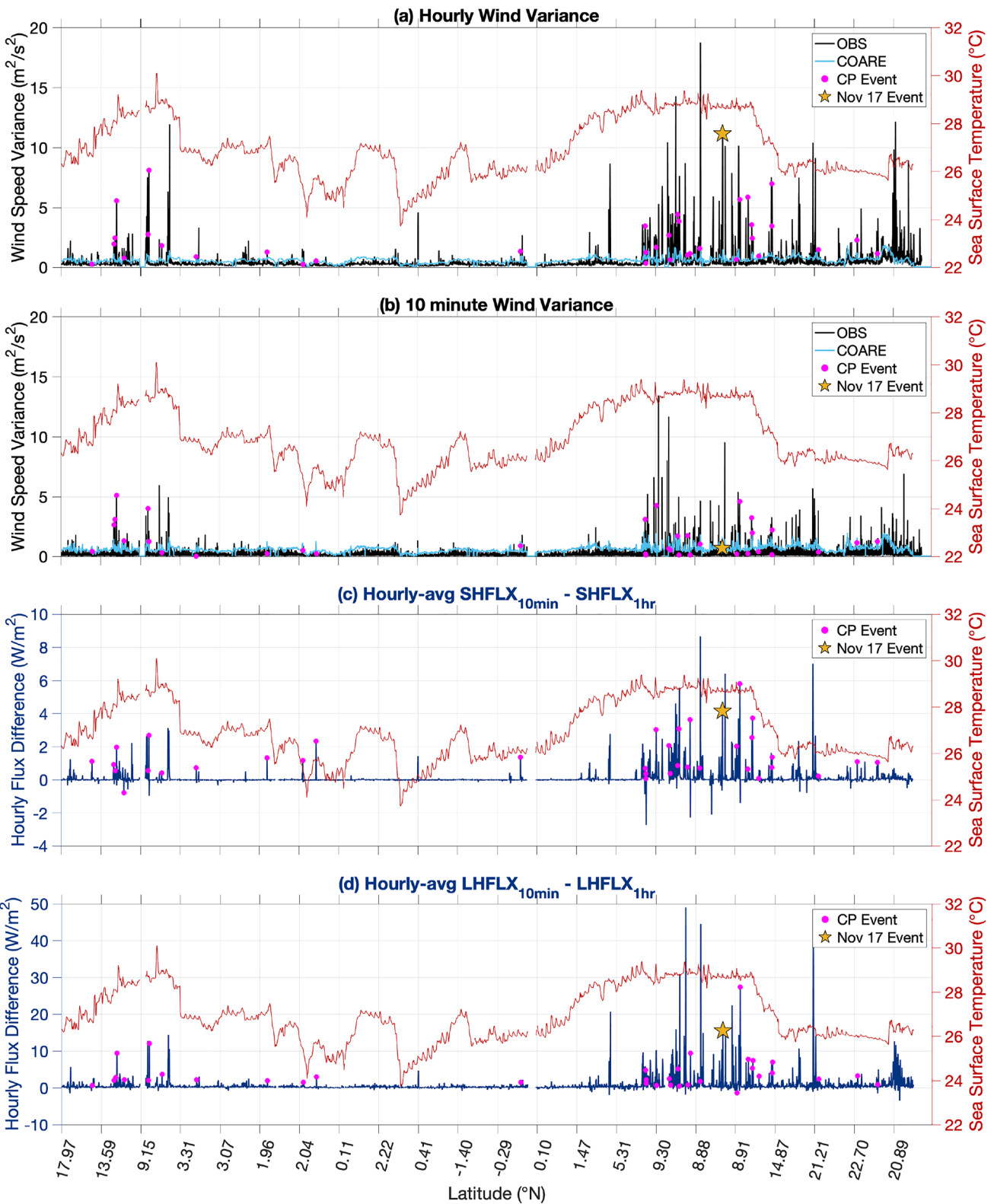


**Figure 7.** SD1069: (Top half, left axes) time series of (a) hourly and (b) 10-min averaged missing wind speed variance based on observations (black lines) and Coupled Ocean-Atmosphere Response Experiment (COARE) 3.5 output (light blue lines). (Bottom half, left axes) time series of hourly-average differences between 10-min and 1-hr bulk (c) sensible and (d) latent heat fluxes from COARE 3.5 output (dark blue lines). (All panels, right axes) time series of hourly-average SST (red lines) observations. Shaded pink circles denote periods when cold pools were detected, and the yellow star marker represents the cold pool case study event on 17 November 2019 from 00:00–01:00 UTC. Note that the time series is linear, but timestamps are replaced with latitude (°N) labels.

To test the sensitivity of the scalar and vector wind speeds to the averaging interval, we evaluate the missing wind variance calculated on 10-min averages, as shown in Figure 7b. Compared to Figure 7a, the results in Figure 7b indicate improved agreement between observations and COARE 3.5 output on 10-min timescales, with missing wind variance reduced to less than  $5 \text{ m}^2/\text{s}^2$  for the majority of convective cold pool events (at least those observed by SD1069). In fact, for the Nov 17 cold pool event, the results are almost identical between the observations and COARE 3.5 output, with missing wind variances of  $0.7 \text{ m}^2/\text{s}^2$  and  $0.6 \text{ m}^2/\text{s}^2$ , respectively. However, within the convectively-active ITCZ (i.e., latitudes where  $\text{SST} > 27.5^\circ\text{C}$ ), there remains large differences up to  $\sim 15 \text{ m}^2/\text{s}^2$ , highlighting the need for 1-min or higher resolution observations of the near-surface wind field to resolve high-frequency variability over select regions of the tropical Pacific.

While the 10-min vector wind does not fully resolve the missing wind variance associated with convective cold pools, it provides key insight on the importance of gustiness for estimating bulk air-sea heat fluxes (Esbensen & McPhaden, 1996). To demonstrate, we apply the COARE 3.5 algorithm to the 10-min and 1-hr averaged data from SD1069 to generate 10-min and 1-hr bulk sensible and latent heat flux time series (not shown). Converting the 10-min flux estimates to 1-hr averages, we compute the differences between the *hourly-averaged* 10-min output and 1-hr output for both sensible and latent heat fluxes, as shown in Figures 7c and 7d, respectively. The results reveal large 1-hr differences in both sensible and latent heat fluxes, with values as high as  $9 \text{ W/m}^2$  and  $50 \text{ W/m}^2$ , respectively. Furthermore, the results indicate that during the November 17 cold pool event, the observed missing wind variance of  $\sim 11 \text{ m}^2/\text{s}^2$  not resolved by the COARE 3.5 algorithm between 00:00–01:00 UTC leads to errors of roughly  $4 \text{ W/m}^2$  in hourly sensible heat flux estimates and  $15 \text{ W/m}^2$  in hourly latent heat flux estimates.

Overall, it is evident that the COARE 3.5 output derived from 1-hr averaged USV measurements underestimates (i.e., positive difference) the bulk flux estimates during convective cold pool events compared to the hourly-average output derived from 10-min averaged measurements. While there are indications that the 1-hr output overestimates sensible and latent heat fluxes mainly within convectively-active regions (i.e., spikes below zero in Figures 7c and 7d), we attribute these results to sporadic missing data points within the respective averaging windows. For example, if a sensor collected 1-min measurements every 5 min, then the 10-min and 1-hr averaged input data would be based on 2 and 12 data points, respectively. In this scenario, it is possible that the missing wind variance would be larger over a 10-min window compared to a 1-hr window. Hence, the negative flux differences are likely an artefact of missing data points, further highlighting the importance of collecting higher resolution (i.e., every minute) measurements. Additionally, the results in Figures 7c and 7d suggest that for high-frequency air-sea phenomena such as convective cold pools, which give rise to highly variable near-surface wind fields, the COARE 3.5 algorithm struggles to fully resolve the gustiness on 10-min timescales, let alone 1-hr timescales. While an evaluation of the gustiness formula used in COARE 3.5 is beyond the scope of the current paper, it would be worthwhile to revisit in future studies to account for convectively-active conditions in tropical ocean regions.

## 6. Discussion and Conclusion

The advent of remotely-piloted platforms for ocean exploration introduces a new era of observing capabilities over remote tropical ocean regions. These new platforms include Sailerone USVs that collect high-resolution, climate-quality observations, which we analyze to explore spatial and temporal scales of air-sea variability associated with convective cold pools over the tropical Pacific ITCZ (defined where  $\text{SST} > 27.5^\circ\text{C}$  north of the equator). As performed in Wills et al. (2021), high-frequency 1-min air temperature time series are used to identify 276 cold pool frontal signatures based on a gradient criteria of  $\leq -1.5^\circ\text{C}$  over a 10-min window, and composite results reveal new insight on the contributing roles of state variables (i.e., temperature, wind, humidity) and physical processes regulating bulk air-sea sensible and latent heat fluxes during these events. A summary of the results is as follows:

- Enhanced latent and sensible heat fluxes peak approximately 10 min after the cold pool temperature front begins, increasing by  $36 \text{ W/m}^2$  and  $23 \text{ W/m}^2$ , respectively, compared to pre-frontal conditions (Figure 3).
- Comparisons of the anomalous 1-min and 10-min flux components (air-sea temperature and moisture gradients and horizontal wind speed) reveal differences in the strength and timing of the temperature and gust fronts, suggesting that 10-min averaged observations do not fully resolve convective cold pool fronts over the ocean (Figure 4).

- A decomposition of the bulk heat flux equations reveals that latent heat flux anomalies are largely regulated by the anomalous wind field acting on the mean background air-sea moisture gradient, while sensible heat flux anomalies are largely regulated by the mean background wind field acting on the anomalous air-sea temperature gradient (Figure 5).

Importantly, the results suggest that the convective cold pool front exerts a mechanical forcing on latent heat fluxes through the anomalous wind field, as well as a thermodynamic forcing on sensible heat fluxes through the anomalous air-sea temperature gradient. Recalling the results of Wills et al. (2021), the anomalous SST field varies by only a few hundredths of a degree during a cold pool passage, indicating that the cold pool itself is driving changes in the anomalous air-sea temperature gradient. Similarly, the air-sea moisture gradient is dominated by changes in the specific humidity field, with the saturation specific humidity also varying by only a few hundredths of g/kg during the frontal passage (not shown). This would indicate that the surge in moisture coincident with the gust front leading edge (Figures 4b and 4c) is entirely driven by the cold pool itself.

We also present a case study of a convective cold pool event observed on 17 November 2019 (Figure 6), to demonstrate how the mobile platforms can be adapted to create traveling mesoscale networks, or “mesonets”, composed of multiple USVs for targeting smaller temporal and spatial scales (<1 day, <100 km) of variability not resolved within existing satellite and GCM footprints. The in situ observations across the mesonet (four drones + TAO buoy) highlight local variations in wind speed and direction associated with the expanding cold pool front across the region, the signature of which is not reflected in the hourly ERA5 reanalysis (or CFSv2 analysis, Figure S1) wind field. With the corresponding 1-min (10-min) time series of wind and air temperature observed by the drones (TAO buoy), the mesonet provides comprehensive information for deriving cold pool properties such as propagation speed and direction, size, location, dissipation statistics, and other physical characteristics. Unlike stationary land-based mesonets, the mobility of saildrone USVs allows for traveling mesonets of varying size and formation to capture different scales of air-sea phenomena across ocean regions.

It should be emphasized that the ability to use multiple Saildrone USVs to form traveling mesonets is a key advantage that sets the drones apart from moored buoy observations. Notwithstanding the mobility of USVs, it can be argued that a single drone at sea operates like that of a TAO buoy, considering that these individual platforms provide point measurements in time. Neither the drones nor the buoys are equipped with rain gauges or radar, thus limiting the ability to detect cold pools to high-frequency variations in temperature, moisture, wind speed and direction, and sea level pressure (Wills et al., 2021, cf. Figure 3). However, in cases of weak cold pools or cold pools at early/late stages of development, it can be difficult to differentiate anomalies in state variables from that of natural variability based on time series alone, thus reducing confidence that a cold pool has been detected by the platforms. In contrast, the increased sampling density afforded by a traveling mesonet provides additional data points necessary to resolve spatiotemporal variability and better infer air-sea phenomena.

Given the availability of 1-min wind speed and velocity measurements, additional analyses were performed to calculate the scalar and vector wind averages based on the definitions in Equations 3 and 4, respectively. Previous studies have found that in regions of low-wind speeds (such as the doldrums of the ITCZ), the vector wind does not properly account for high-frequency wind variations, requiring the addition of a gustiness parameter to resolve bulk air-sea heat fluxes (Cronin et al., 2006; Edson et al., 2013; Esbensen & McPhaden, 1996; Fairall et al., 1996, 2003; Godfrey & Beljaars, 1991). As the squared gustiness (or missing wind variance) relates to the scalar and vector winds per Equation 5, we were able to use the 1-min wind speed measurements collected on SD1069 to directly calculate the missing wind variance on 1-hr and 10-min timescales, providing a basis for comparison against the COARE 3.5 gustiness output. The results from SD1069 revealed large differences in missing wind variance within the convectively-active ITCZ for both 1-hr and 10-min averages, with the latter displaying improved agreement between the observed and COARE 3.5 estimates (Figures 7a and 7b). Interestingly, the reduced missing wind variance in the 10-min averaged data corresponds to larger bulk sensible and latent heat flux estimates on hourly timescales compared to that derived from 1-hr averaged data (Figures 7c and 7d), emphasizing the importance of resolving the scalar versus vector wind field.

Figure 8 provides an overview of the 1-hr and 10-min average missing wind variance as a function of vector wind magnitude derived from all available USV observations during the 2017–2019 TPOS missions. There is significant spread in the relationship between vector wind speed and missing wind variance, with variances as high as 50 m<sup>2</sup>/s<sup>2</sup> and 30 m<sup>2</sup>/s<sup>2</sup> for the 1-hr (Figure 8a) and 10-min (Figure 8b) vector wind averages, respectively. The majority of convective cold pool events (denoted by pink circles) appear to be associated with vector

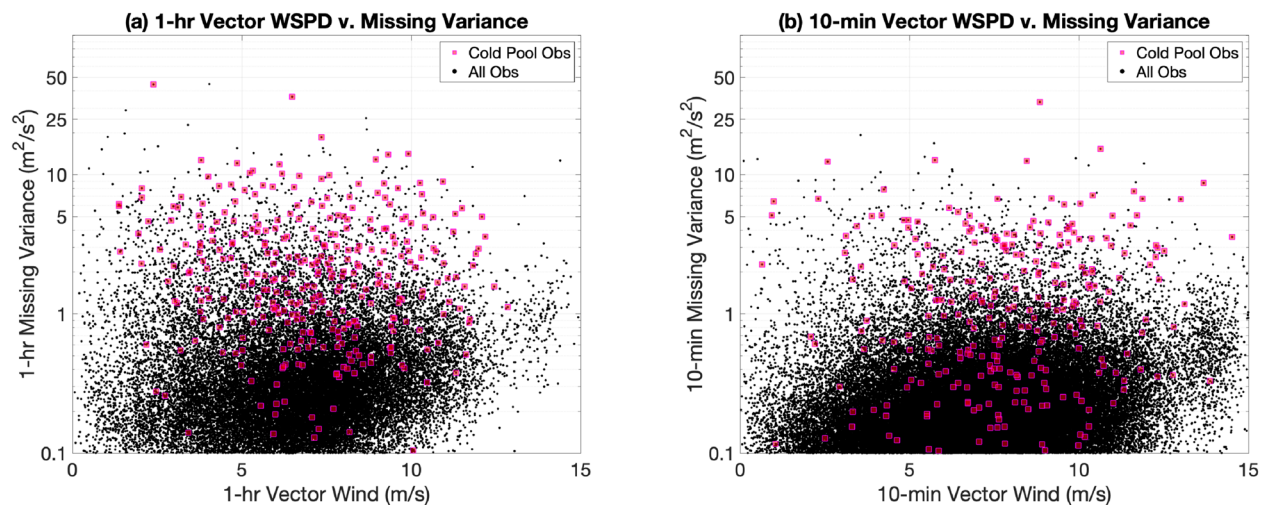


**Figure 8.** Scatter plot of (a) 1-hr vector wind speed versus 1-hr missing wind speed variance and (b) 10-min vector wind speed versus 10-min missing wind speed variance based on measurements from 10 Saildrone USVs during the 2017, 2018, and 2019 missions. Shaded pink squares denote 1-hr and 10-min windows in panels (a and b), respectively, when a cold pool event was detected.

wind speeds ranging from 5 to 10 m/s regardless of the averaging interval. However, similar to the results in Figure 7b, it is qualitatively evident from Figure 8b that missing wind variance associated with cold pool events is reduced for the 10-min vector winds compared to the 1-hr vector winds. This suggests that the 10-min vector winds better represent the 10-min scalar winds, although there remains room for improvement in the presence of high-frequency variability as evident in the composite results in Figure 4c, which indicate that the 10-min averaged wind speed observations underestimate the strength of the cold pool gust front by almost half compared to the 1-min measurements.

Recalling the flux decomposition results in Figure 5, variations in wind and temperature are dominant factors influencing bulk latent and sensible heat fluxes, respectively. While we explored gustiness (and missing wind variance) on different averaging intervals between saildrone USV observations and COARE 3.5 output, we did not explore how gustiness is parameterized in bulk formulas. In the COARE 3.5 algorithm, gustiness is largely a function of the buoyancy flux, which is partially derived from the air-sea temperature gradient (Edson et al., 2013; Fairall et al., 2003). Depending on the sign of the buoyancy flux, the gustiness parameter is either derived from input fields or assigned a minimum constant value. Considering the large variations in the temperature field associated with the frontal passage, it is likely that the sign and magnitude of the air-sea temperature gradient are sensitive to the averaging interval, similar to the scalar and vector wind fields. Future analyses will focus on high-frequency variations in the air-sea temperature field and the implications for calculating the gustiness parameter and bulk sensible heat fluxes in the COARE 3.5 algorithm. Additional studies will utilize high-resolution saildrone USV observations to investigate new methods for parameterizing gustiness in bulk algorithms, with emphasis on convectively-active environments.

### Data Availability Statement

Saildrone data used in this study are provided by NOAA/PMEL Ocean Climate Stations Project Office of NOAA/PMEL (OCS Project Office, 2017) and available for download at <https://www.pmel.noaa.gov/ocs/sail-drone/data-access>. TAO data used in this study are provided by the GTMBA Project Office of NOAA/PMEL (GTMBA Project Office, 2019) and available for download at <https://www.pmel.noaa.gov/tao/drupal/disdell/>. The GPM IMERG data used in this study were provided by the NASA/Goddard Space Flight Center's Precipitation Measuring Mission and Precipitation Processing System (Huffman et al., 2019) and archived at <https://disc.gsfc.nasa.gov/datasets>. The ERA5 global reanalysis data used in this study were generated using Copernicus Climate Change Service information 2022 (Hersbach et al., 2018) and is available for download at <https://doi.org/10.24381/cds.adbb2d47>. The NCEP CFSv2 analysis data used in this study were generated using the Research Data Archive at NCAR Computational and Information Systems Laboratory (Saha et al., 2011) and is available



for download at <https://doi.org/10.5065/D6N877VB>. Figures were made with MATLAB version 9.14.0 (The MathWorks Inc, 2023), available at <https://www.mathworks.com>, and M\_Map version 1.4m (Pawlowicz, 2020), available at <https://www.eoas.ubc.ca/~rich/map.html>.

### Acknowledgments

We thank Dr. Leah D. Grant and Nicholas M. Falk, as well as one anonymous reviewer, for their insightful and helpful comments that have improved the overall manuscript. The authors thank Saildrone, Inc. for their piloting and engineering efforts and for providing additional seadays during the 2017, 2018, and 2019 Saildrone Missions. This work was supported by NOAA's Global Ocean Monitoring and Observing Program, NOAA's Climate Program Office/Climate Variability and Predictability Program, NOAA's Office of Marine and Aviation Operations, and NOAA's Office of Ocean Exploration and Research. This publication is partially funded by the Cooperative Institute for Climate, Ocean, & Ecosystem Studies (CIOCES) under NOAA Cooperative Agreement NA20OAR4320271, Contribution No. 2022-1235, and is PMEL Publication No. 5425.

### References

- Benjamin, T. B. (1968). Gravity currents and related phenomena. *Journal of Fluid Mechanics*, *31*(2), 209–248. <https://doi.org/10.1017/s0022112068000133>
- Betts, A. K., & Silva Dias, M. F. (1979). Unsaturated downdraft thermodynamics in cumulonimbus. *Journal of the Atmospheric Sciences*, *36*(6), 1061–1071. [https://doi.org/10.1175/1520-0469\(1979\)036<1061:UDTIC>2.0.CO;2](https://doi.org/10.1175/1520-0469(1979)036<1061:UDTIC>2.0.CO;2)
- Bowman, K. P., Collier, J. C., North, G. R., Wu, Q., Ha, E., & Hardin, J. (2005). Diurnal cycle of tropical precipitation in tropical rainfall measuring mission (TRMM) satellite and ocean buoy rain gauge data. *Journal of Geophysical Research*, *110*(D21), D21104. <https://doi.org/10.1029/2005jd005763>
- Brilouet, P.-E., Redelsperger, J.-L., Bouin, M.-N., Couvreur, F., & Lebeaupin Brossier, C. (2021). A case-study of the coupled ocean–atmosphere response to an oceanic diurnal warm layer. *Quarterly Journal of the Royal Meteorological Society*, *147*(736), 2008–2032. <https://doi.org/10.1002/qj.4007>
- Brock, F. V., Crawford, K. C., Elliott, R. L., Cuperus, G. W., Stadler, S. J., Johnson, H. L., & Eilts, M. D. (1995). The Oklahoma mesonet: A technical overview. *Journal of Atmospheric and Oceanic Technology*, *12*(1), 5–19. [https://doi.org/10.1175/1520-0426\(1995\)012<0005:TOMATO>2.0.CO;2](https://doi.org/10.1175/1520-0426(1995)012<0005:TOMATO>2.0.CO;2)
- Byers, H. R., & Braham, R. R. (1949). *The thunderstorm: Report of the thunderstorm project*. US Government Printing Office.
- Chandra, A. S., Zuidema, P., Krueger, S., Kochanski, A., de Szoeko, S. P., & Zhang, J. (2018). Moisture distributions in tropical cold pools from equatorial Indian Ocean observations and cloud-resolving simulations. *Journal of Geophysical Research: Atmospheres*, *123*(20), 11–445. <https://doi.org/10.1029/2018JD028634>
- Charba, J. (1974). Application of gravity current model to analysis of squall-line gust front. *Monthly Weather Review*, *102*(2), 140–156. [https://doi.org/10.1175/1520-0493\(1974\)102<0140:AOGCMT>2.0.CO;2](https://doi.org/10.1175/1520-0493(1974)102<0140:AOGCMT>2.0.CO;2)
- Chuda, T., Niino, H., Yoneyama, K., Katsumata, M., Ushiyama, T., & Tsukamoto, O. (2008). A statistical analysis of surface turbulent heat flux enhancements due to precipitating clouds observed in the tropical western pacific. *Journal of the Meteorological Society of Japan. Ser. II*, *86*(3), 439–457. <https://doi.org/10.2151/jmsj.86.439>
- Cronin, M. F., Fairall, C. W., & McPhaden, M. J. (2006). An assessment of buoy-derived and numerical weather prediction surface heat fluxes in the tropical pacific. *Journal of Geophysical Research*, *111*(C6), C06038. <https://doi.org/10.1029/2005jc003324>
- Dai, A. (2001). Global precipitation and thunderstorm frequencies. PART II: Diurnal variations. *Journal of Climate*, *14*(6), 1112–1128. [https://doi.org/10.1175/1520-0442\(2001\)014<1112:gpatfp>2.0.co;2](https://doi.org/10.1175/1520-0442(2001)014<1112:gpatfp>2.0.co;2)
- de Szoeko, S. P., Marke, T., & Brewer, W. A. (2021). Diurnal Ocean surface warming drives convective turbulence and clouds in the atmosphere. *Geophysical Research Letters*, *48*(4), e2020GL091299. <https://doi.org/10.1029/2020GL091299>
- de Szoeko, S. P., Skillingstad, E. D., Zuidema, P., & Chandra, A. S. (2017). Cold pools and their influence on the tropical marine boundary layer. *Journal of the Atmospheric Sciences*, *74*(4), 1149–1168. <https://doi.org/10.1175/JAS-D-16-0264.1>
- Drager, A. J., & van den Heever, S. C. (2017). Characterizing convective cold pools. *Journal of Advances in Modeling Earth Systems*, *9*(2), 1091–1115. <https://doi.org/10.1002/2016ms000788>
- Edson, J. B., Jampana, V., Weller, R. A., Bigorre, S. P., Plueddemann, A. J., Fairall, C. W., et al. (2013). On the exchange of momentum over the open ocean. *Journal of Physical Oceanography*, *43*(8), 1589–1610. <https://doi.org/10.1175/jpo-d-12-0173.1>
- Engerer, N. A., Stensrud, D. J., & Coniglio, M. C. (2008). Surface characteristics of observed cold pools. *Monthly Weather Review*, *136*(12), 4839–4849. <https://doi.org/10.1175/2008MWR2528.1>
- Esbensen, S. K., & McPhaden, M. J. (1996). Enhancement of tropical ocean evaporation and sensible heat flux by atmospheric mesoscale systems. *Journal of Climate*, *9*(10), 2307–2325. [https://doi.org/10.1175/1520-0442\(1996\)009<2307:eoteoa>2.0.co;2](https://doi.org/10.1175/1520-0442(1996)009<2307:eoteoa>2.0.co;2)
- Fairall, C. W., Bradley, E. F., Hare, J., Grachev, A. A., & Edson, J. B. (2003). Bulk parameterization of air–sea fluxes: Updates and verification for the coare algorithm. *Journal of Climate*, *16*(4), 571–591. [https://doi.org/10.1175/1520-0442\(2003\)016<0571:bpoasf>2.0.co;2](https://doi.org/10.1175/1520-0442(2003)016<0571:bpoasf>2.0.co;2)
- Fairall, C. W., Bradley, E. F., Rogers, D. P., Edson, J. B., & Young, G. S. (1996). Bulk parameterization of air–sea fluxes for tropical ocean–global atmosphere coupled-ocean atmosphere response experiment. *Journal of Geophysical Research*, *101*(C2), 3747–3764. <https://doi.org/10.1029/95jc03205>
- Feng, Z., Hagos, S., Rowe, A. K., Burleyson, C. D., Martini, M. N., & de Szoeko, S. P. (2015). Mechanisms of convective cloud organization by cold pools over tropical Warm Ocean during the AMIE/DYNAMO field campaign. *Journal of Advances in Modeling Earth Systems*, *7*(2), 357–381. <https://doi.org/10.1002/2014MS000384>
- Fournier, M. B., & Haerter, J. O. (2019). Tracking the gust fronts of convective cold pools. *Journal of Geophysical Research: Atmospheres*, *124*(21), 11103–11117. <https://doi.org/10.1029/2019jd030980>
- Garg, P., Nesbitt, S. W., Lang, T. J., & Pfrift, G. (2021). Diurnal cycle of tropical oceanic mesoscale cold pools. *Journal of Climate*, *34*(23), 9305–9326. <https://doi.org/10.1175/jcli-d-20-0909.1>
- Garg, P., Nesbitt, S. W., Lang, T. J., Pfrift, G., Chronis, T., Thayer, J. D., & Hence, D. A. (2020). Identifying and characterizing tropical oceanic mesoscale cold pools using spaceborne scatterometer winds. *Journal of Geophysical Research: Atmospheres*, *125*(5), e2019JD031812. <https://doi.org/10.1029/2019JD031812>
- Gentine, P., Garelli, A., Park, S.-B., Nie, J., Torri, G., & Kuang, Z. (2016). Role of surface heat fluxes underneath cold pools. *Geophysical Research Letters*, *43*(2), 874–883. <https://doi.org/10.1002/2015GL067262>
- Glickman, T. S., & Zenk, W. (2000). *Glossary of meteorology* (2nd ed.). AMS (American Meteorological Society).
- Godfrey, J., & Beljaars, A. (1991). On the turbulent fluxes of buoyancy, heat and moisture at the air–sea interface at low wind speeds. *Journal of Geophysical Research*, *96*(C12), 22043–22048. <https://doi.org/10.1029/91jc02015>
- Goff, R. C. (1976). Vertical structure of thunderstorm outflows. *Monthly Weather Review*, *104*(11), 1429–1440. [https://doi.org/10.1175/1520-0493\(1976\)104<1429:vsoto>2.0.co;2](https://doi.org/10.1175/1520-0493(1976)104<1429:vsoto>2.0.co;2)
- Grant, L. D., Lane, T. P., & van den Heever, S. C. (2018). The role of cold pools in tropical oceanic convective systems. *Journal of the Atmospheric Sciences*, *75*(8), 2615–2634. <https://doi.org/10.1175/JAS-D-17-0352.1>
- Grant, L. D., & van den Heever, S. C. (2016). Cold pool dissipation. *Journal of Geophysical Research: Atmospheres*, *121*(3), 1138–1155. <https://doi.org/10.1002/2015JD023813>

- Gray, W. M., & Jacobson, R. W., Jr. (1977). Diurnal variation of deep cumulus convection. *Monthly Weather Review*, *105*(9), 1171–1188. [https://doi.org/10.1175/1520-0493\(1977\)105<1171:dvodcc>2.0.co;2](https://doi.org/10.1175/1520-0493(1977)105<1171:dvodcc>2.0.co;2)
- GT MBA Project Office. (2019). Global tropical moored buoy array [Dataset]. National Oceanographic and Atmospheric Administration, Pacific Marine Environmental Laboratory, Global Tropical Moored Buoy Array Data Display and Delivery. Retrieved from <https://www.pmel.noaa.gov/tao/drupal/disdel/>
- Haerter, J. O., & Schlemmer, L. (2018). Intensified cold pool dynamics under stronger surface heating. *Geophysical Research Letters*, *45*(12), 6299–6310. <https://doi.org/10.1029/2017gl076874>
- Hersbach, H., Bell, B., Berrisford, P., Biavati, G., Horányi, A., Muñoz-Sabater, J., et al. (2018). ERA5 hourly data on single levels from 1979 to present [Dataset]. Copernicus Climate Change Service (C3S) Climate Data Store (CDS). <https://doi.org/10.24381/cds.adbb2d47>
- Hersbach, H., Bell, B., Berrisford, P., Hirahara, S., Horányi, A., Muñoz-Sabater, J., et al. (2020). The ERA5 global reanalysis. *Quarterly Journal of the Royal Meteorological Society*, *146*(730), 1999–2049. <https://doi.org/10.1002/qj.3803>
- Houze, R. A. (1977). Structure and dynamics of a tropical squall-line system. *Monthly Weather Review*, *105*(12), 1540–1567. [https://doi.org/10.1175/1520-0493\(1977\)105<1540:sadoat>2.0.co;2](https://doi.org/10.1175/1520-0493(1977)105<1540:sadoat>2.0.co;2)
- Huffman, G. J., Bolvin, D. T., Braithwaite, D., Hsu, K., Joyce, R., Xie, P., & Yoo, S.-H. (2015). NASA global precipitation measurement (GPM) integrated multi-satellite retrievals for GPM (IMERG). Algorithm Theoretical Basis Document (ATBD) Version, 4 (p. 26).
- Huffman, G. J., Stocker, E. F., Bolvin, D. T., Nelkin, E. J., & Tan, J. (2019). GPM IMERG final precipitation L3 half hourly 0.1 degree x 0.1 degree V06 [Dataset]. Goddard Earth Sciences Data and Information Services Center. <https://doi.org/10.5067/GPM/IMERG/3B-HH/06>
- Joseph, J., Girishkumar, M., McPhaden, M., & Rao, E. P. R. (2021). Diurnal variability of atmospheric cold pool events and associated air-sea interactions in the Bay of Bengal during the summer monsoon. *Climate Dynamics*, *56*(3–4), 837–853. <https://doi.org/10.1007/s00382-020-05506-w>
- Kilpatrick, T. J., & Xie, S.-P. (2015). Ascet observations of downdrafts from mesoscale convective systems. *Geophysical Research Letters*, *42*(6), 1951–1958. <https://doi.org/10.1002/2015GL063025>
- Lafore, J.-P., & Moncrieff, M. W. (1989). A numerical investigation of the organization and interaction of the convective and stratiform regions of tropical squall lines. *Journal of the Atmospheric Sciences*, *46*(4), 521–544. [https://doi.org/10.1175/1520-0469\(1989\)046<0521:ANIOTO>2.0.CO;2](https://doi.org/10.1175/1520-0469(1989)046<0521:ANIOTO>2.0.CO;2)
- Langhans, W., & Romps, D. M. (2015). The origin of water vapor rings in tropical oceanic cold pools. *Geophysical Research Letters*, *42*(18), 7825–7834. <https://doi.org/10.1002/2015GL065623>
- Large, W., & Yeager, S. (2009). The global climatology of an interannually varying air–sea flux data set. *Climate Dynamics*, *33*(2), 341–364. <https://doi.org/10.1007/s00382-008-0441-3>
- Li, Z., Zuidema, P., & Zhu, P. (2014). Simulated convective invigoration processes at trade wind cumulus cold pool boundaries. *Journal of the Atmospheric Sciences*, *71*(8), 2823–2841. <https://doi.org/10.1175/JAS-D-13-0184.1>
- McPhaden, M. J., Busalacchi, A. J., & Anderson, D. L. (2010). A toga retrospective. *Oceanography*, *23*(3), 86–103. <https://doi.org/10.5670/oceanog.2010.26>
- McPhaden, M. J., Busalacchi, A. J., Cheney, R., Donguy, J.-R., Gage, K. S., Halpern, D., et al. (1998). The tropical ocean–global atmosphere observing system: A decade of progress. *Journal of Geophysical Research*, *103*(C7), 14169–14240. <https://doi.org/10.1029/97JC02906>
- Moncrieff, M. W., & Liu, C. (1999). Convection initiation by density currents: Role of convergence, shear, and dynamical organization. *Monthly Weather Review*, *127*(10), 2455–2464. [https://doi.org/10.1175/1520-0493\(1999\)127<2455:cibder>2.0.co;2](https://doi.org/10.1175/1520-0493(1999)127<2455:cibder>2.0.co;2)
- OCS Project Office. (2017). OCS TPOS saildrone missions [Dataset]. National Oceanographic and Atmospheric Administration, Pacific Marine Environmental Laboratory, Ocean Climate Stations Saildrone Data Access. Retrieved from <https://www.pmel.noaa.gov/ocs/saildrone/data-access>
- Pawlowicz, R. (2020). M\_Map: A mapping package for Matlab [Software]. Computer Software. Matlab. Retrieved from <https://www.eoas.ubc.ca/~rich/map.html>
- Rochetin, N., Hohenegger, C., Touzé-Peiffer, L., & Vilefranco, N. (2021). A physically based definition of convectively generated density currents: Detection and characterization in convection-permitting simulations. *Journal of Advances in Modeling Earth Systems*, *13*(7), e2020MS002402. <https://doi.org/10.1029/2020ms002402>
- Ross, A., Tompkins, A. M., & Parker, D. (2004). Simple models of the role of surface fluxes in convective cold pool evolution. *Journal of the Atmospheric Sciences*, *61*(13), 1582–1595. [https://doi.org/10.1175/1520-0469\(2004\)061<1582:SMOTRO>2.0.CO;2](https://doi.org/10.1175/1520-0469(2004)061<1582:SMOTRO>2.0.CO;2)
- Saha, S., Moorthi, S., Wu, X., Wang, J., Nadiga, S., Tripp, P., et al. (2011). NCEP climate forecast system version 2 (CFSv2) selected hourly time-series products [Dataset]. Research Data Archive at the National Center for Atmospheric Research, Computational and Information Systems Laboratory. <https://doi.org/10.5065/D6N877VB>
- Saha, S., Moorthi, S., Wu, X., Wang, J., Nadiga, S., Tripp, P., et al. (2014). The NCEP climate forecast system version 2. *Journal of Climate*, *27*(6), 2185–2208. <https://doi.org/10.1175/jcli-d-12-00823.1>
- Saxen, T. R., & Rutledge, S. A. (1998). Surface fluxes and boundary layer recovery in toga coare: Sensitivity to convective organization. *Journal of the Atmospheric Sciences*, *55*(17), 2763–2781. [https://doi.org/10.1175/1520-0469\(1998\)055<2763:SFABLR>2.0.CO;2](https://doi.org/10.1175/1520-0469(1998)055<2763:SFABLR>2.0.CO;2)
- Schiro, K. A., & Neelin, J. D. (2018). Tropical continental downdraft characteristics: Mesoscale systems versus unorganized convection. *Atmospheric Chemistry and Physics*, *18*(3), 1997–2010. <https://doi.org/10.5194/acp-18-1997-2018>
- Serra, Y. L. (2018). Precipitation measurements from the tropical moored array: A review and look ahead. *Quarterly Journal of the Royal Meteorological Society*, *144*(S1), 221–234. <https://doi.org/10.1002/qj.3287>
- Serra, Y. L., & McPhaden, M. J. (2004). In situ observations of diurnal variability in rainfall over the tropical Pacific and Atlantic Oceans. *Journal of Climate*, *17*(18), 3496–3509. [https://doi.org/10.1175/1520-0442\(2004\)017<3496:ISOODV>2.0.CO;2](https://doi.org/10.1175/1520-0442(2004)017<3496:ISOODV>2.0.CO;2)
- Simoes-Sousa, I. T., Tandon, A., Buckley, J., Sengupta, D., Sree Lekha, J., Shroyer, E., & Szoek, S. P. d. (2023). Atmospheric cold pools in the Bay of Bengal. *Journal of the Atmospheric Sciences*, *80*(1), 167–180. <https://doi.org/10.1175/JAS-D-22-0041.1>
- Simpson, J. (1969). A comparison between laboratory and atmospheric density currents. *Quarterly Journal of the Royal Meteorological Society*, *95*(406), 758–765. <https://doi.org/10.1002/qj.49709540609>
- Skyllingstad, E. D., & de Szoek, S. P. (2015). Cloud-resolving large-eddy simulation of tropical convective development and surface fluxes. *Monthly Weather Review*, *143*(7), 2441–2458. <https://doi.org/10.1175/MWR-D-14-00247.1>
- Tanimoto, Y., Nakamura, H., Kagimoto, T., & Yamane, S. (2003). An active role of extratropical sea surface temperature anomalies in determining anomalous turbulent heat flux. *Journal of Geophysical Research*, *108*(C10), 3304. <https://doi.org/10.1029/2002jc001750>
- Terai, C. R., & Wood, R. (2013). Aircraft observations of cold pools under marine stratocumulus. *Atmospheric Chemistry and Physics*, *13*(19), 9899–9914. <https://doi.org/10.5194/acp-13-9899-2013>
- The MathWorks Inc. (2023). MATLAB version: 9.14.0 (R2023a) [Software]. The MathWorks Inc. Retrieved from <https://www.mathworks.com>
- Tomita, H., Hihara, T., Kako, S., Kubota, M., & Kutsuwada, K. (2019). An introduction to j-ofuro3, a third-generation Japanese ocean flux data set using remote-sensing observations. *Journal of Oceanography*, *75*(2), 171–194. <https://doi.org/10.1007/s10872-018-0493-x>

- Tompkins, A. M. (2001). Organization of tropical convection in low vertical wind shears: The role of cold pools. *Journal of the Atmospheric Sciences*, 58(13), 1650–1672. [https://doi.org/10.1175/1520-0469\(2001\)058<1650:OOTCIL>2.0.CO;2](https://doi.org/10.1175/1520-0469(2001)058<1650:OOTCIL>2.0.CO;2)
- Torri, G., Kuang, Z., & Tian, Y. (2015). Mechanisms for convection triggering by cold pools. *Geophysical Research Letters*, 42(6), 1943–1950. <https://doi.org/10.1002/2015GL063227>
- van den Heever, S. C., Grant, L. D., Freeman, S. W., Marinescu, P. J., Barnum, J., Bukowski, J., et al. (2021). The Colorado state university convective cloud outflows and updrafts experiment (c3 loud-ex). *Bulletin of the American Meteorological Society*, 102(7), E1283–E1305. <https://doi.org/10.1175/bams-d-19-0013.1>
- Wakimoto, R. M. (1982). The life cycle of thunderstorm gust fronts as viewed with Doppler radar and rawinsonde data. *Monthly Weather Review*, 110(8), 1060–1082. [https://doi.org/10.1175/1520-0493\(1982\)110<1060:tlcotg>2.0.co;2](https://doi.org/10.1175/1520-0493(1982)110<1060:tlcotg>2.0.co;2)
- Wang, W., & McPhaden, M. J. (2000). The surface-layer heat balance in the equatorial Pacific Ocean. Part II: Interannual variability. *Journal of Physical Oceanography*, 30(11), 2989–3008. [https://doi.org/10.1175/1520-0485\(2001\)031<2989:tslhbh>2.0.co;2](https://doi.org/10.1175/1520-0485(2001)031<2989:tslhbh>2.0.co;2)
- Williams, A. G. (2001). A physically based parametrization for surface flux enhancement by gustiness effects in dry and precipitating convection. *Quarterly Journal of the Royal Meteorological Society*, 127(572), 469–491. <https://doi.org/10.1002/qj.49712757212>
- Wills, S. M., Cronin, M. F., & Zhang, D. (2021). Cold pools observed by uncrewed surface vehicles in the central and eastern tropical Pacific. *Geophysical Research Letters*, 48(10), e2021GL093373. <https://doi.org/10.1029/2021gl093373>
- Yang, H., Liu, J., Lohmann, G., Shi, X., Hu, Y., & Chen, X. (2016). Ocean-atmosphere dynamics changes associated with prominent ocean surface turbulent heat fluxes trends during 1958–2013. *Ocean Dynamics*, 66(3), 353–365. <https://doi.org/10.1007/s10236-016-0925-3>
- Young, G. S., Perugini, S. M., & Fairall, C. W. (1995). Convective wakes in the equatorial western Pacific during TOGA. *Monthly Weather Review*, 123(1), 110–123. [https://doi.org/10.1175/1520-0493\(1995\)123<0110:CWITEW>2.0.CO;2](https://doi.org/10.1175/1520-0493(1995)123<0110:CWITEW>2.0.CO;2)
- Zhang, D., Cronin, M. F., Meinig, C., Farrar, J. T., Jenkins, R., Peacock, D., et al. (2019). Comparing air-sea flux measurements from a new unmanned surface vehicle and proven platforms during the spurs-2 field campaign. *Oceanography*, 32(2), 122–133. <https://doi.org/10.5670/oceanog.2019.220>
- Zipser, E. J. (1969). The role of organized unsaturated convective downdrafts in the structure and rapid decay of an equatorial disturbance. *Journal of Applied Meteorology and Climatology*, 8(5), 799–814. [https://doi.org/10.1175/1520-0450\(1969\)008<0799:troouc>2.0.co;2](https://doi.org/10.1175/1520-0450(1969)008<0799:troouc>2.0.co;2)
- Zuidema, P., Torri, G., Muller, C., & Chandra, A. (2017). A survey of precipitation-induced atmospheric cold pools over oceans and their interactions with the larger-scale environment. *Surveys in Geophysics*, 38(6), 1283–1305. <https://doi.org/10.1007/s10712-017-9447-x>